The Pore Structure of Indiana Limestone and Pink Dolomite for the Modeling of Carbon Dioxide in Geologic Carbonate Rock Formations

by

Marina Freire-Gormaly

A thesis submitted in conformity with the requirements
for the degree of Masters of Applied Science

Department of Mechanical and Industrial Engineering
University of Toronto

UMI Number: 1570770

UMI

Dissertation Publishing

UMI 1570770

ProQuest

www.manaraa.com

The Pore Structure of Indiana Limestone and Pink Dolomite for the Modeling of Carbon Dioxide in Geologic Carbonate Rock Formations

Marina Freire-Gormaly

Masters of Applied Science

Department of Mechanical and Industrial Engineering
University of Toronto

2013

Abstract

The primary objective was to predict the relative storage capacity of carbonate rocks relevant for carbon dioxide sequestration. To achieve this, a detailed pore scale characterization of model carbonate rocks, Indiana Limestone and Pink Dolomite, was conducted utilizing micro-computed tomography (microCT) data using pore network modeling and invasion percolation simulations. For the first time in literature, Pink Dolomite's pore space characteristics were analyzed. A secondary objective was to compare thresholding techniques as applied to carbonates which exhibit dual porosity (porosity at multiple length scales). The analysis showed the sensitivity of existing methods to the thresholding technique, imaging method and material. Overall, the contributions of this work provide an assessment of two carbonates relevant for carbon capture and storage at the pore scale; and a preliminary assessment into thresholding dual porosity carbonates.

Acknowledgments

I extend my sincere gratitude to everyone who helped me throughout this process. In particular, I would like to thank my supervisors, Prof. Aimy Bazylak and Prof. Heather MacLean, for their expert guidance, constructive feedback, and extended efforts, all of which ensured the success of this endeavour. I would like to thank Dr. Jon Ellis for all of his help, learning the fundamentals of pore network modeling, SciNet, and MATLAB, and providing helpful feedback on various revisions. I would also like to thank James Hinebaugh for his support in learning the nuances of the pore network model. As well, I would like to thank the lab for all of their help, support and comradery. I would also like to thank Bryan Tatone for his support collecting the microCT data. George Kretschmann provided very useful guidance in learning how to operate the SEM equipment. I would also like to extend my sincere gratitude to my family and friends, whose generous and unrelenting support was invaluable. Finally, I would like to thank Carbon Management Canada, and the University of Toronto for their generous financial support, and encouragement through the annual conferences, and professional development opportunities. Finally, I dedicate this work to my grandparents, who were always encouraging and supportive.

Table of Contents

List of Tables

List of Figures

Abbreviations & Nomenclature

Acronyms

microCT	X-ray micro-computed tomography
REV	representative elementary volume
SEM	scanning electron microscopy

Variables

n	number of incident rays
P_c	capillary pressure
r	radius
r_{pore}	pore radius
V_{pore}	pore volume
V_{bulk}	total material volume

Greek Letters

α	contact angle
φ	porosity
θ	angle of incidence
λ	wavelength
$\varnothing$	diameter
γ	surface tension

Chapter 1

Introduction

1.1   Background

Carbon dioxide sequestration, also known as carbon capture and storage is recognized by the Intergovernmental Panel on Climate Change as a promising method to lower carbon dioxide emissions from concentrated sources, such as coal power plants, or oil refineries [1]. A major subset of carbon capture and storage methods involves the injection of carbon dioxide into deep geologic media (greater than 800 m below surface [2]). In order to safely, and securely store the carbon dioxide for generations to come, microscale studies on the transport of carbon dioxide through porous media are required. In particular, developing accurate numerical models to predict the saturation profiles of dissolved carbon dioxide, and its migration through the geosphere requires detailed characterization of the rock structure below the centimeter scale. Describing the migration patterns and improvements to the predictability of the flow regime requires a pore scale characterization of the rock structures where the carbon dioxide is injected.

Micro-computed tomography (microCT) is a powerful tool for characterizing, in three dimensions, the internal structure of rock core samples through non-destructive examination. The collected data is used to extract a pore network model, which is a geometrical representation of the pore space as a series of pores connected by throats [3]. The pore network model provides the fundamental pore scale structure of the rocks, in terms of the pore size distribution, throat radius distribution, pore coordination number (representing the connectivity of the pores to one another), and the pore-to-pore distance. The invasion of a fluid through the material can then be simulated through invasion percolation simulations to determine the rock's permeability (ability to permit flow). This information is crucial to the development of realistic characterizations of the pore geometry and saturation profiles that lead to improved system scale simulations.

MicroCT and the extracted pore network models have been used extensively for petroleum [4, 5] and geologic [6, 7] studies to characterize the pore geometry, permeability and porosity of sandstone [4, 8-10] and oil-bearing carbonates [11-15] to

determine the potential productivity of oil reservoirs and to enhanced oil recovery [16]. However, microCT and pore network models have seen limited application to carbonates for use in carbon sequestration studies.

There are two primary carbonate formations in North America where carbon dioxide is injected to enhance oil recovery, specifically in the Weyburn Fields in Saskatchewan, Canada, and in the Permian Basin in Texas, USA [16, 17]. Bachu [18] identified the Alberta Basin as an ideal location for carbon dioxide sequestration due to the geologic suitability, high porosity formations with low permeability caprock, as well as the proximity to large carbon dioxide emitters. However, despite this preliminary study of the Alberta Basin much work remains to fully analyze the detailed microstructure and multiphase transport parameters of suitable carbonate reservoirs [17]. Their heterogeneous porosity (defined as dual porosity) and permeability distributions [17] add a complexity not found in sandstone formations, requiring further in depth investigation. Indiana Limestone and Pink Dolomite reasonably represent the porosity and permeability conditions identified for sequestration in the Alberta basin [10] and can be taken as representative model carbonates.

For dual porosity rocks, such as carbonates, it is challenging to capture the full range of the pore structure with a single imaging technique due to pore sizes over a broad range (nanometres to centimetres) [19-21]. Deriving relationships between the porosity and flow-based properties for carbonate reservoirs remains an area of active research, due mainly to the complexity of carbonate structures because of their dual porosity [21-31]. Some researchers [32, 33] have used image registration techniques [29] (which involves the use of multiple images at various resolutions) to combine high resolution data from scanning electron microscopy (SEM) with lower resolution microCT data. Image registration techniques, however, are dependent on computationally intensive algorithms [29] to combine the porosity data at disparate length scales. To overcome this challenge, most recently, Ji et al. [20] proposed a methodology to determine the microporosity directly from microCT data of Indiana Limestone. However, it has seen limited application to other carbonates. To determine the porosity of rocks from microCT or SEM data, the greyscale images need to be converted to binary images (representing rock space and pore space) through a process called thresholding. The literature lacks a systematic

thresholding technique applicable broadly to microCT and SEM data of carbonates.

1.2 Motivation

The immediate motivation for this thesis is the pressing need for an accurate numerical model that characterizes carbonate rocks relevant for carbon capture and storage at the microscale with a realistic and valid description of the rock structure as a pore network. To accomplish this requirement, model carbonate rock samples need to be analyzed in detail for their physical porous characteristics. The characteristics can then provide a generic description of the rock's pore space as input into the numerical modeling of the geological rock formation under study.

This work also derives from its relevance to the broader objectives of the research being conducted at the University of Toronto, University of British Columbia, University of Alberta and the University of Calgary for Carbon Management Canada, under 'Project B04: A pore scale microlab to perform fundamental laboratory-based studies of carbon dioxide transport and reactivity in reservoirs.' Researchers in this project are working on developing innovative numerical methods and experimental setups to emulate core conditions in geologic carbon dioxide sequestration. The data collected from this research will help facilitate the modeling of the rock structure from the microscale level to the reservoir scale.

1.3 Objectives

The overall objective of this thesis is to predict the relative storage capacity of carbonate rock formations by characterizing the porous structure of two model carbonate rocks relevant for carbon dioxide sequestration; Indiana Limestone and Pink Dolomite through pore network modeling and invasion percolation simulations. A secondary objective is to provide a comparison of thresholding techniques of SEM and microCT data as applied to Indiana Limestone and Pink Dolomite in order to determine the sensitivity of thresholding techniques to the imaging technique, spatial resolution, and material.

1.4 Contributions

The thesis has led to the following contributions:

Pore Structure Characterization

- Statistical distributions of pore scale parameters describing the internal pore geometry were determined for two model carbonate rocks, Indiana Limestone and Pink Dolomite, which are representative of suitable geological formations for carbon dioxide storage. These statistical distributions are necessary as structural input parameters for pore scale and reservoir scale simulations of carbon dioxide injection into brine-filled porous rock structures to determine the carbon dioxide storage capacities of these formations. The key characteristics of the pore space that were determined include: mean pore volume, mean pore radius, mean throat radius, mean coordination number, and mean pore-to-pore distance.

- The log-normal distributions of the pore space parameters were found using a pore space extraction scheme based on the Watershed algorithm. The distributions for Indiana Limestone match well with the literature with as small as a 9 % difference. This work presents the first pore scale description of Pink Dolomite, as there is little discussion in literature on this carbonate.

- From pore space extractions based on microCT imaging and a novel Watershed algorithm, Pink Dolomite's and Indiana Limestone's pore structure and saturation profiles were determined for use in future upscaling studies to ultimately support reservoir scale modeling.

Mineral Characterization

- The bulk mineral composition of Indiana Limestone and Pink Dolomite were determined using X-ray fluorescence as 98.6 % and 99.4 % calcite ($CaCO_3$) by atomic weight percent, respectively.

Dual Porosity of Carbonates

- High-resolution (0.9-1.5 μm/pixel) SEM images were compared to the lower resolution three-dimensional microCT image data to determine the sensitivity of thresholding methods to the imaging technique, spatial resolution and material.

- For Indiana Limestone, the porosity determined using single Otsu, Ji et al.'s [20] dual Otsu and the high resolution SEM image was (13±1) %, (14±4) % and (23±4) %, respectively. For Pink Dolomite, the porosity determined using single Otsu, Ji et al.'s [20] dual Otsu and the high resolution SEM image was (30±2) %, (27±2) % and (34±3) %, respectively.

1.5   Organization of the Thesis

This thesis is organized into five chapters. In this first chapter, a general introduction, motivation, objectives and contributions are provided. Chapter 2 provided a literature review on carbon capture and storage methods and discussed the experimental and numerical approaches for characterizing the rock structures found in the literature. In Chapter 3, the pore structure characterization studies, both experimental and numerical, which were conducted on four Indiana Limestone and four Pink Dolomite rock samples are presented and discussed. In Chapter 4, the assessment of thresholding techniques to characterize the dual porosity of the Indiana Limestone and Pink Dolomite samples are provided. In Chapter 5, the conclusions and the recommendations for future work are detailed.

Chapter 2
Background and Literature Review

2.1   Introduction

In this chapter carbon sequestration in deep geologic formations (greater than 800 m below surface [2]) is introduced and a description of the transport of carbon dioxide through porous media is presented. Previous studies on the transport of carbon dioxide through rock media, both experimental and numerical, are discussed. An overview of pore network modeling and previous studies with modeling of rock structures is reviewed.

2.2   Carbon Dioxide Sequestration in Geologic Media

Carbon dioxide sequestration in geologic media, also known as carbon capture and storage is recognized by the Intergovernmental Panel on Climate Change as a promising method to reduce carbon dioxide emissions from the combustion of coal, and natural gas [1]. Carbon capture and storage has received much attention for its potential for mitigating carbon dioxide emissions from large industrial emitters, such as power plants, which use coal, oil, natural gas, and industrial facilities producing hydrogen, and ammonia, pulp and paper plants, cement production and petrochemical refineries.

A carbon capture and storage system has three main components, the capture of the carbon dioxide from the facility, the transportation of the carbon dioxide to the injection site, and its storage in a suitable geologic formation. Although the technology exists to perform each of these three main components, there remain challenges in transitioning carbon capture and storage to wide-spread use. The injection of carbon dioxide is in commercial use for enhanced oil recovery, yet remains an area of active research [19, 34-36]. Methods for storing the carbon dioxide include mineralization in mine effluents, storage in the oceanic crust, and underground storage.

Currently, there are numerous sites with demonstration projects for carbon dioxide storage in deep geologic formations. Some of the major demonstration projects are Sleipner in Norway, Weyburn in Saskatchewan, In Salah in Algeria, and Snøhvit in Norway, (see

Table 2-1) [37]. These projects provide valuable field data and demonstrate the feasibility of carbon capture and storage methods. However, further investigations are required to predict the migration of the injected carbon dioxide plume, and overall capacity of storage sites. Despite the promise of carbon capture and storage, long-term safety of the injected carbon dioxide, costs, and ensuring stored carbon dioxide remains subsurface are challenges that need to be overcome to enable wide-scale implementation of the technology. In particular, characterizing the geologic structures into which the carbon dioxide is injected remains an important challenge in accurately modeling the movement of carbon dioxide in over thousands of years.

2.3   Carbon Dioxide Sequestration in Saline Aquifers

One promising class of geological formations suitable for long-term carbon dioxide storage is deep underground saline aquifers. Their relative global abundance [38, 39], proximity to large greenhouse gas emitters [38, 39], and distance from drinking water basins [40] make them a suitable location for carbon dioxide storage. Depending on the specific geologic formation, saline aquifers can be found at depths between 800 m and 5000 m below the surface [1]. The injection of carbon dioxide occurs at pressures above 7.83 MPa [41]. Close to the injection well, the forces dominating the flow are viscous while beyond the injection well, the forces dominating the transport are capillary. In this regimen, Darcy's flow is applicable.

Recently, deep saline limestone aquifers have been identified as suitable storage reservoirs for carbon dioxide sequestration in the Sunniland Trend within the Sunniland Formation in Florida, owing to their high porosity and adequate hydrocarbon stratigraphic trapping [16, 42]. There remain challenges in estimating the long-term safety of the injected carbon within the porous rocks. Primarily, assurances are required that the carbon dioxide will remain trapped and will not migrate to the surface or contaminate groundwater [18, 43, 44]. Reservoir scale analyses are conducted to estimate the

migration of the carbon dioxide plume within the geological formation [45]. These reservoir scale estimations of carbon dioxide transport require a detailed knowledge of its behavior at the pore scale, which in turn depends on the porous structure of the target geological formation [46, 47]. To determine the suitability of a specific geologic formation, microscale studies are required to identify the detailed rock structure, to understand how carbon dioxide will flood the rock and interact with *in situ* brine, and to determine the eventual mineralization of the trapped carbon [48].

The first rocks considered for carbon dioxide sequestration by both industry and researchers were sandstone formations. This is because sandstone reservoirs hold a large portion of global petroleum [49] and have been the location for enhanced oil recovery projects and carbon dioxide sequestration pilot projects [50]. As a result, significant information exists on their pore scale characterization and the microscale behavior of injected carbon dioxide within sandstone reservoirs [11, 12, 36, 49-52]. However, interest in sequestration in carbonate rocks is quite recent and detailed characterization is required.

To date, there are two primary carbonate formations in North America in which enhanced oil recovery is conducted using carbon dioxide injection, specifically in the Weyburn Fields in Saskatchewan, Canada, and in the Permian Basin in Texas, USA [16, 17]. Bachu [18] identified the Alberta Basin as an ideal location for carbon dioxide sequestration due to the geologic suitability, high porosity formations with low permeability caprock, as well as the proximity to large carbon dioxide emitters, including power plants and cement producers. However, despite this preliminary study of the Alberta Basin much work remains to fully analyze the detailed microstructure and multiphase transport parameters of suitable carbonate reservoirs [17]. Their heterogeneous porosity and permeability distributions [17] add a complexity not found in sandstone formations, requiring further in depth investigation. Indiana Limestone and Pink Dolomite reasonably represent the porosity and permeability conditions identified for sequestration in the Alberta basin [10] and can be taken as representative model carbonates. The microstructures of Pink Dolomite and Indiana Limestone require detailed characterization, in order to accurately model the complex geochemical processes that occur during carbon sequestration [20, 53, 54]. Although the bulk properties of Dolomite

[55] and Indiana Limestone [56] are known, it is necessary to examine samples of these rocks in detail, in order to develop a robust database that can confidently describe the rock microstructure as an input to numerical simulations of the geologic system.

2.4   Experimental Techniques to Determine Porous Microstructure of Rocks

Knowledge of the pore structure is necessary for determining the carbon dioxide storage capacity of a geologic formation. To characterize the microstructure of rocks, a number of experimental and numerical techniques have been applied in the literature. These include thin-section analysis [57], scanning electron microscopy (SEM) [57, 58], focused ion beam microscopy-SEM [59], and mercury intrusion porosimetry [12, 21, 60, 61]. These techniques are destructive, so downstream measurements are not possible, and results for multiple techniques must be averaged across multiple samples.

Micro-computed tomography (microCT) is a non-destructive technique for assessing the three-dimensional internal geometry of porous structures [62, 63]. The primary advantage is the ability of the technique to image at the micron scale volumes of material including bones and rocks. The sample is rotated through 360° and exposed to an X-ray beam at minute increments. The projections of the X-ray beam passing through the sample are assembled into a three-dimensional greyscale representation. The greyscale values of the three-dimensional image are correlated to the linear attenuation of the X-ray beam through the sample. The sample's varying density and the atomic number of the materials in the sample attenuate the incoming beam. Since the sample must be fully exposed to the beam, there is a physical limit to the sample size, which is inversely proportional to the image resolution. The two-dimensional images captured at successive angular rotations are combined using image processing software to reveal the internal structure of the material after the greyscale images are converted to binary images.

MicroCT has been used extensively for petroleum [4, 5] and geologic [6, 7] studies to structurally characterize sandstone [4, 8-10] and oil-bearing carbonates [11, 12] to determine the potential productivity of oil reservoirs and enhanced oil recovery [16]. To analyze the pore space of a porous material, the three-dimensional grayscale data from microCT needs to be converted to a numerical representation, called a pore network model. A pore network model consists of pores that represent the sample voids and

throats connecting the pores [3]. The process of determining the pore network model is called extraction, and first involves the division of the grayscale data into a binary image data set followed by geometrical interpretation of the binary data into pores and throats. Subsequently, the permeability and pore structure geometry can be measured [13-15]. However, this technique has seen limited application to carbonates for use in carbon sequestration studies. Carbonates are particularly challenging to characterize due to the processes which occur after the rocks have formed, such as mineral dissolution and precipitation, which result in large pores (in the range of millimetres in diameter), and channels of varying connectivity [64].

The experimental techniques described above, have been used extensively in the literature. Hollis et al. [60] analysed a database of over 100 thin sections from core plugs of the North Oman oilfield, located in the Sultanate of Oman, which is a carbonate reservoir formation, and combined the thin-section analysis with mercury intrusion porosimetry analysis of a database of over 2600 core plugs to ground the typing of rocks in both petrographic analyses and the microscale pore geometry. Although this study provided detailed petrographic analysis, and a thorough assessment of the oilfield, it did not provide an analysis of the three-dimensional microstructure information. Jiang et al. [15] used extracted three-dimensional images of sandstones to validate an innovative extraction algorithm. This study found the permeability values of the extracted network differed significantly from those calculated using the Lattice-Boltzmann methodology, indicating further refinements were required.

Machado et al. [65] used microCT to validate its ability to measure porosity effectively for carbonates at various resolutions. Their study did not perform network extractions to determine other rock parameters, such as coordination number, permeability or features of the geometric topography. Bera et al. [66] investigated the presence of nanopores within the porous structure of Berea Sandstone using focused-ion-beam-SEM. They concluded nanopores are present on the order of $2000nm^3$ in a $9.45\mu m^3$ volume, with good connectivity to the bulk pore space [66]. Their study lacked an analysis of the pore network and the impact the addition of nanopores had on the overall permeability of the rocks.

Padhy et al. [64] combined back-scattered electron-SEM, statistical image analysis, nuclear magnetic resonance and mercury intrusion porosimetry techniques to statistically characterize the structure of Berea Sandstone and synthetic samples at multiple length scales. Their study was primarily focused on the validation of the nuclear magnetic resonance technique and they concluded that further refinements were required due to discrepancies between the simulated networks and the mercury intrusion porosimetry results. Their study lacked an alternate means of computing the permeability curves through a pore network invasion percolation assessment to resolve the discrepancies between the simulated networks and the mercury intrusion porosimetry results.

Zhu et al. [31] performed a thin-section analysis of Indiana Limestone core samples and found pore radii in the range (25-50) μm. While Gharbi et al. [67] and Bijeljic et al. [30] determined the mean pore radius of Indiana Limestone to be (10 μm). This indicates the technique used to measure the pore radius can influence the measured value.

While thin-section analysis, SEM and focused-ion-beam-SEM can provide two-dimensional images of the microstructure, microCT is the only experimental technique which can provide high spatial resolution data in three-dimensions. The collected data needs to be interpreted and analyzed using pore network models, and can then provide detailed information on the pore geometry, and permeability. The literature lacks an analysis of Pink Dolomite, while the analysis of Indiana Limestone from the literature can provide a set of comparative values.

2.5 Porosity of Carbonate Rocks

The porosity of a sample is a measure of the void volume [68]. Porosity is a key parameter required to determine the permeability and to predict macroscopic transport properties for bulk reservoir modeling [69]. The total porosity (φ) of a rock sample is defined as follows:

$$\varphi = \frac{V_{pore}}{V_{bulk}} \qquad (2.2)$$

where V_{pore} represents the volume of the pores, and V_{bulk} represents the total volume of the material including the pore space. The φ can be determined directly from a binary image

stack of the sample volume, as in microCT. The porosity can also be measured using a number of techniques including: helium pycnometry, mercury intrusion, wet weight vs. dry weight and imaging techniques [68]. However, helium pycnometry, and wet weight vs. dry weight techniques can only access the pores which are connected to the exterior edges of the sample [70].

2.5.1   Thresholding

To convert the grayscale images to black-and-white images, a threshold is used to separate the porous material into two distinct regions, void and material. For porous materials that have a uniform pore size, such as sandstones, or materials with a high-contrast between the material and the pore space, the division into a binary image is a trivial process. Otsu's method [71] is a commonly applied thresholding technique [20, 30, 67, 72-74]. In Otsu's method, the grayscale histogram is iteratively tested in order to minimize the spread (also called variance) of the distributions above and below the threshold. The grayscale value which minimizes the variance is selected as the threshold. However, for materials with non-uniform pore sizes, such as carbonates, determining the threshold is not a straightforward process. The conversion of the image into its pore space and material is a critical stage [20, 67, 74, 75], since an incorrect segmentation can lead to an over- or under-estimation of the pore space.

2.5.2   Dual Porosity of Carbonates

Dual porosity refers to a void volume with porous features across multiple length scales. For dual porosity rocks such as carbonates it is challenging to capture the full range of the pore structure with a single imaging technique due to pore sizes over a broad range (nanometres to centimetres) [19-21]. Deriving relationships between the porosity and flow based properties for carbonate reservoirs remains an area of active research, due mainly to the complexity of carbonate structures because of their dual porosity [21-31]. Dual porosity is characterized by both an apparent macroporosity, having features well above the spatial resolution of microCT imaging, and microporosity with features near or below the microCT resolution. As a result, the estimation of transport properties such as permeability and tortuosity, is more challenging since correlations, such as Archie's Law, are no longer applicable [76]. Further, characterizing the dual porosity is in itself a

challenge, since the pore sizes range from nanometers [66] to centimeters [77]. A single imaging technique cannot visualize pore sizes across disparate length scales, so the use of multiple imaging techniques is required [36, 37]. As well, microCT data is required due to the three-dimensional representation of the pore space, while SEM data is only on a two-dimensional plane of the sample.

Because carbonates exhibit porosity below the resolution of the microCT (defined as microporosity) some researchers [32, 33] have used image registration techniques [29] (which involves the use of multiple images at various resolutions) to combine high resolution data from SEM with the lower resolution microCT data. However, to perform image registration large data sets of SEM data are required. To overcome this challenge, most recently, Ji et al. [20] proposed a correlation for determining the microporosity directly from microCT data. Ji et al.'s [20] correlation is based on the relationship between the grayscale value of a voxel and the attenuation of the X-ray through the material. Ji et al. [20] applied dual thresholding to an Indiana Limestone sample to determine the volume which was below the resolution of the microCT. Their technique worked well for greyscale histogram data exhibiting dual Gaussian peaks. However, it has seen limited application to other carbonates. A key gap in the literature on dual porosity carbonates is there lacks a systematic thresholding technique applicable broadly to microCT and SEM data.

2.6   Pore Network Modeling for Geologic materials

Pore network extraction and modeling is used in porous material research to simplify the structure of a sample void space into a digital form that can be analyzed to determine geometric properties (e.g., pore radius, pore volume, pore coordination number, and pore-to-pore distance, described in Table 2-2) of the material [25, 72, 74, 79-82]. A pore network model consists of pores that represent the sample voids and throats connecting them [3]. Pore network extraction techniques can be used to characterize the microstructure of volumetric imaging data and identify detailed geometric information regarding the pore space. These geometric parameters can then be input directly into pore scale transport studies [24, 29, 30, 57, 67, 83] or as averaged grid-based values for reservoir scale modeling [10, 84, 85].

Until recently, pore network models of rock materials relied on thin-sectioning and laborious processing of hundreds of individual slices of information [12]. However, microCT allows for rapid processing of the internal three-dimensional structure of the porous material, down to voxel resolutions of 1 μm for small samples [20, 21, 24, 29]. A voxel is a three-dimensional pixel, while the pixel is the smallest unit of a two-dimensional image.

Pore network models have been used extensively in geology and petrology to investigate the pore morphology of rocks, and to study invasion patterns and transport parameters on imaged pore structure [75, 79, 86-90]. The determination of pore locations is achieved through a few common methods: grain-based and voxel-based. In the grain-based approach, material centers are identified as grain locations, which then establish adjacent pore locations. From this skeleton, the connectivity and the pore morphology can be determined [6, 25, 91, 92]. With the voxel-based technique, the maximum inscribed radius within the void space is used to determine the radius of associated pores [6, 75, 88, 93, 94]. Hence, the pore radius provides an underestimate of the pore volume. The throat radius is the inscribed sphere at the constriction between two pores. The pore coordination number is a representation of the connectivity of the pores to each another. A higher pore coordination number implies a better connected network of pores. The pore-to-pore distance is the shortest distance between two pores. The pore volume, pore radius, throat radius, pore coordination, and pore-to-pore distance are shown graphically in Table 2-2. A full review of the work conducted in pore network modeling for geologic porous media can be found at [80, 95].

Although the grain and voxel methods are effective in producing a pore network model of the material, considerable improvements have been made in reducing computation time through the use of the Watershed algorithm [96]. This algorithm segments the void structure based on how it would be invaded by water [97]. An advantage is that this technique requires fewer computations than grain- or voxel-based approaches. As a result, a larger sample volume can be studied [72].

Gharbi et al. [67] and Bijeljic et al. [30] used pore network modeling to investigate four sandstones and two carbonates, one of which was Indiana Limestone. Their algorithm

however, had a geometric constraint, which limits the number of possible connections to a given pore. This can lead to unphysical representations of the pore space since in the porous material there are no arbitrary limits on the interconnections between void spaces. Hinebaugh et al. [98] developed a novel pore network extraction technique that built on existing studies of geologic materials [99-102] without a geometric constraint. However, Hinebaugh et al.'s [98] pore network model had not been applied to Indiana Limestone and Pink Dolomite.

2.7 Invasion Percolation

Invasion percolation simulations have been used extensively to determine the saturation and capillary pressure profiles of geologic materials [79, 103-106]. Invasion percolation simulations are performed on an extracted pore network to determine the capillary pressure vs. saturation curves of the investigated geologic material. Invasion percolation simulations are performed using the Washburn equation in the capillary flow regime [107].

The Washburn equation describes the pressure required to breakthrough a narrow cylindrical passage, such as the throats of the pore network model. In Equation 3.2, the capillary pressure is written as follows:

$$P_c = \frac{2\gamma}{r}\cos\alpha \quad (2.3)$$

where P_c (Pascals) is the capillary pressure required for a liquid with surface tension γ (Newtons per meter) to penetrate a cylindrical tube with radius r (m), and the contact angle between the material and the invading liquid is given by α (radians). In invasion percolation simulations the pore network is invaded with the operating fluid. The pore space is continuously filled until saturation occurs. At each iteration, a given pore is filled as long as the pressure is sufficiently large to enter.

2.8 Experimental Techniques to Determine Mineral Composition

Knowledge of the mineral composition is required for performing invasion percolation simulations, as the contact angle between the invading fluid and the solid matrix is required [31]. The mineral composition of core samples can be determined through a

variety of methods, including X-ray diffraction spectrometry [36], X-ray fluorescence [36, 108] and scanning electron microscopy with electron dispersive spectroscopy [109]. X-ray diffraction spectrometry and X-ray fluorescence are bulk techniques, whereas SEM with electron dispersive spectroscopy can determine the chemical composition at the microscale. These techniques are all destructive.

X-ray fluorescence spectrometry is reliant on Bragg's Law to deduce the overall frequency of the chemical composition. It relies on the diffraction of a collimated X-ray beam off of a sample. The approach relies on the angle of scattering off a sample due to Bragg's Law

$$n\lambda = 2d \sin \theta \qquad (2.1)$$

where n is an integer count of the number of incident waves, λ (meters) is the wavelength of the incident ray, d (meters) is the spacing between the atomic lattice, and θ (radians) is the angle between the scattered waves and the incident wave.

X-ray fluorescence spectrometry works on the principle of ionization of elements resulting in the emission of electrons at energies correlated to the elemental composition in weight percent [110]. The investigated material, in a powdered and pressed sample holder is subjected to a collimated X-ray beam that excites the orbital electrons, which are subsequently emitted. The emitted waves scatter and are counted by a detector. The frequency at which the scattered waves impact the detector, as the sample is passed through a 360° rotation, indicates the percentage by weight of the sample's chemical composition. X-ray fluorescence spectrometry provides a detailed elemental mineral composition of the bulk sample [110].

Scanning electron microscopy uses a high energy electron beam to interact with a conductive specimen [111]. The electron beam is decelerated by the specimen and can be visualized using secondary electrons emitted from the sample as in back-scattered electrons, or using photons, as in electron dispersive spectroscopy. In SEM-electron dispersive spectroscopy, specific microscale features of the sample can be analyzed for their chemical composition [58].

2.9   Conclusion
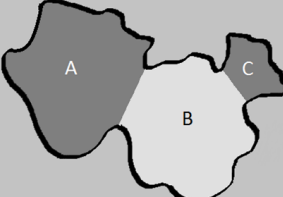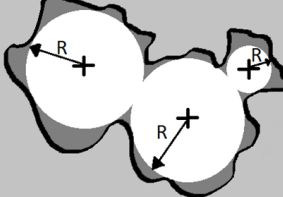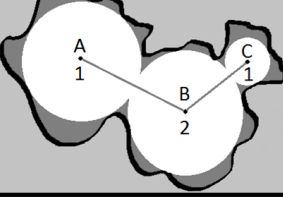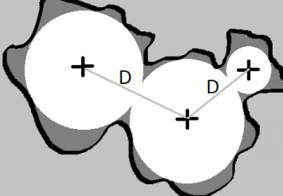
In this chapter, a review of the experimental and numerical techniques to investigate the mineral and pore structure of geologic materials was presented. Though the pore structure of Indiana Limestone and numerous other rocks have been reported in literature, there is a lack of data on Pink Dolomite. A systematic method to quantify the dual porosity of carbonates is also absent from literature.

2.10 Tables

Table 2-1: Major carbon capture and storage projects globally for post combustion capture. The year in parentheses indicates the year the project began operation. Projects selected from major deep geologic sequestration sites summarized from [37].

Project	Location	Company Leading the Project	Storage Type	Depth (m)	Approximate Storage of Carbon Dioxide per year (Millions of Tonnes)
Sleipner (1996)	North Sea, Norway	Statoil	Offshore Deep Saline Formation	850	1
Weyburn (2000)	Saskatchewan, Canada	Pan Canadian	Enhance Oil Recovery	2000	2.7
In Salah (2004)	Algeria	BP	Onshore Deep Saline Formation	2000	1
Snøhvit (2008)	Barents Sea, Norway	Statoil	Offshore Deep Saline Formation	2600	0.7

Table 2-2: Summary of the pore space characteristics of a pore network model.

Pore Space Characteristic	Graphical Description	Explanation
Pore Volume		A, B, C are the pore names. The pore volume is the full region in the pore.
Pore Radius		Pore radius (R) is the radius of the largest inscribed sphere within a pore volume.
Throat Radius		Throat radius (T) is the radius of the constriction between two pore volumes.
Pore Coordination Number		Pore coordination counts the number of pores connected to a given pore.
Pore-to-Pore Distance		Pore-to-pore distance (D) is the shortest distance between two pores.

Chapter 3

Pore Structure Characterization of Indiana Limestone and Pink Dolomite from Pore Network Reconstructions

3.1   Introduction

Challenges remain in estimating the storage capacity of formations and the long-term safety of the injected carbon within the porous rocks [18, 43, 44]. Reservoir scale analyses can be conducted to estimate the migration of the carbon dioxide plume within the geology [45]; however, these reservoir scale studies require estimates of upscaled transport properties for the target formation, which are ultimately governed by effects at the pore scale [46, 47]. To determine these pore scale parameters, microscale studies are required to identify the detailed rock structure, to understand how carbon dioxide will flood the rock and interact with *in situ* brine, and to determine the eventual stability of trapped carbon [48]. This study presented in this chapter contributes a detailed pore scale characterization of carbonate rocks.

Although sandstone reservoirs have been well characterized in the literature [12, 49, 50, 52] because they contain a large portion of global petroleum reserves [49], studies are required for saline aquifers of limestone and dolomite. These rocks have been identified as suitable carbon dioxide sequestration targets due to their high porosity and effective stratigraphic trapping [16, 42]. In contrast to sandstones, the complex microstructure of carbonates [29] requires a more in-depth investigation.

Bachu [18] has identified the Alberta Basin, a carbonate geological formation, as an ideal location for carbon dioxide sequestration for its high porosity formations capped with low permeability caprock. Despite this preliminary study of the Alberta Basin, much work remains to fully characterize the detailed microstructure and multiphase transport parameters of suitable carbonate reservoirs [17]. For this study, physical samples from Alberta basin formations could not be obtained due to existing property and licensing rights in the region. Instead, model carbonate samples were acquired. Indiana Limestone

and Pink Dolomite were chosen to reasonably represent the porosity and permeability conditions identified for sequestration in the Alberta basin [10].

Developing a detailed characterization of limestone and dolomite microstructures is necessary for accurate modeling of the complex geochemical processes involved in carbon dioxide sequestration in carbonate formations [10, 18]. Limestone and dolomite form the main structural components of carbonate saline aquifers. Although the bulk properties of many dolomites [55] and limestones [56] are known, a detailed examination of the microstructure is necessary to develop a robust methodology to characterize the carbonate geology.

To characterize the microstructure of rocks, a number of experimental and numerical techniques have been applied in the literature. These include thin-section analysis [57], scanning electron microscopy (SEM) [57, 58], focused ion beam-SEM [59], and mercury intrusion porosimetry [12, 21, 60, 61]. These techniques are destructive, so downstream measurements are not possible, and results for multiple techniques must be averaged across multiple samples.

In contrast, X-ray micro-computed tomography (microCT), is a non-destructive technique for volumetric characterization, which has been used extensively to image porous materials in three-dimensions [62, 63, 112]. This facilitates subsequent analyses, such as pore network modeling to determine the characteristics of the pore space. Similarly, the porosity can be measured directly from a binary image stack of the sample volume [25].

Pore network extraction and modeling is used in porous material research to simplify the structure of a sample void space into a formalism that can be analyzed in various ways [25, 72, 74, 79-82]. A pore network model consists of pores that represent the sample's voids and the throats connecting the pores [3]. Pore network extraction techniques can be used to characterize the porous structures imaged using microCT to identify detailed geometric information regarding the pore space.

Zhu et al. [31] performed a thin-section analysis of Indiana Limestone core samples and found pore radii in the range (25-50) μm. Although Zhu et al. [31] studied Indiana Limestone their investigation was at a resolution of ~33 μm due to the minimum

thickness of the thin-section. Gharbi et al. [67] and Bijeljic et al. [30] performed pore network modeling on microCT data of four sandstones and two carbonates, including Indiana Limestone at a resolution of 7.7 µm per voxel. Although they were able to characterize the microstructure of Indiana Limestone, a key gap was that they did not examine Pink Dolomite, and that they used a pore network model which had geometrical constraints, meaning limits were placed on the number of throats a pore could have. Hinebaugh et al. [98] developed a novel pore network extraction technique that built on existing studies of geologic materials [99-102] and improved the tessellation process by accounting for overlapping pores and including trapped air phases. In contrast to the work of Gharbi et al. [67] and Bijeljic et al. [30] the pore network model of Hinebaugh et al. [98] had no geometrical constraint. This leads to a better physical representation of the rock pore space since no limit was placed on the number of possible connections to a given pore.

The following geometric properties; porosity, pore size, pore radius, throat radius, pore coordination number, and the pore-to-pore distance are required to describe the microstructure of the pore space [113]. The porosity is a measure of the void volume of the sample, including both the connected and unconnected pores of the sample. The pore size distributions are statistical measure of the pores in the sample. The pore radius is the radius of the inscribed sphere in the pore network extraction of the pore space. The throat radius is the radius of the cylindrical throats which connect pores. The pore coordination number represents the connectivity of the pore space. The pore-to-pore distance is the shortest distance between two given pore centers. To assess the transport parameters, knowledge of the mineral composition is necessary for performing the invasion percolation simulations, as the contact angle between the invading fluid and the solid matrix is required [31].

The two main objectives of the experimental and numerical work discussed in this chapter are to first characterize the internal microporous structure and second to begin to assess the transport parameters of the model carbonate cores.

3.2   Methodology

The experimental and analytical methods used to determine the microstructure of Indiana Limestone and Pink Dolomite are detailed below.

3.2.1   Selection, Preparation and Mineral Characterization of the Rocks

Two geological cores of Indiana Limestone and Pink Dolomite were selected as model carbonates for the carbon dioxide storage technology analysis. These samples were selected based on their relevance as model carbonates representative of the North Alberta Basin [10], and consistent with the requirements for a suitable carbon dioxide storage site outlined in [2] based on guidelines from the Intergovernmental Panel on Climate Change [1], and the European Union's best practice guidelines for carbon capture and storage technology [114]. All rock cores were obtained from Kocurek Industries (Caldwell, TX, USA). Their characterization, as provided by the supplier, is summarized in Table 3-1.In this study, microCT was selected to image the three-dimensional structure of the samples because it provides a digital representation of the volumetric pore space at a high spatial resolution. Similarly, the microCT data is ideal for subsequent pore network extraction to characterize the microstructure of the rock samples. The characteristics crucial for evaluating a given rock's suitability for carbon dioxide storage are the pore volume, pore radius, throat radius, pore coordination number, and the pore-to-pore distance.

To choose the sample size, it was essential to select a volume such that the pore space investigated was representative of the rock structure at a larger scale. The representative elementary volume (REV) is the minimum sample volume required to obtain an accurate measurement of a desired property (porosity, permeability or tortuosity). Selection of the sample REV depends on the property being measured and the porous material investigated – for sandstones, measurement of permeability generally requires an REV at least twice as large as that for determining the porosity [115].

A full scale assessment of the REV of carbonate dolostones for porosity was conducted by De Boever et al. [25] on microCT data with a spatial resolution of 1.5 μm^3/voxel. They determined the REV to be 0.07 mm^3. In contrast, Mostaghimi et al. [115] showed that the REV was larger than their carbonate sample sizes of 4 mm^3 for both permeability and

porosity when the spatial resolution of their microCT data was 5 μm^3/voxel, due to pore scale heterogeneity. This indicates that a lower spatial resolution requires a larger sample REV and carbonates have a large REV for permeability. For these reasons, the datasets collected in this work were chosen to be the largest possible size for spatial resolutions below 11 μm^3/voxel. This enabled detection of the macropores within the sample, and will allow for future investigations into the permeability and tortuosity of the pore space. The sample sizes were selected to be at minimum 66.5 mm^3 for the Indiana Limestone samples, and 53.5 mm^3 for the Pink Dolomite samples.

The two cores were sectioned into five cylindrical samples 1cm x 0.6 ($\varnothing$) cm (approx.) using a dremel tool prior to scanning. Cutting with a dremel can be destructive to the edges of the samples; however, the edges were cropped during image processing. Four samples of Indiana Limestone and four samples of Pink Dolomite were studied using microCT. One sample of Indiana Limestone and one sample of Pink Dolomite were analyzed using SEM, the results and discussion can be found in Chapter 4.

X-ray fluorescence was chosen to determine the mineral composition because it provides the relative amount of each chemical component of the bulk mineral composition [36, 108]. X-ray fluorescence spectroscopy was conducted with a Philips PW2404 (Philips Corporation, Amsterdam, The Netherlands) in the Geology Laboratory, Department of Earth Sciences (University of Toronto). The samples were individually ground to a fine powder using a ceramic mortar and pestle, then pelletized and placed in the sample holder.

3.2.2   MicroCT Imaging and Processing Techniques

The microCT imaging was performed using a General Electric Phoenix v|tome|x s machine (General Electric, Connecticut, United States of America) in the Geomechanics Laboratory (Civil Engineering, University of Toronto). The microCT machine was equipped with a 180kV / 15 W high-power nano-focus X-ray tube housed within a protective radiation safety cabinet. A voxel is the smallest unit of a three-dimensional image, while the pixel is the smallest unit of a two-dimensional image. Voxel resolutions between 7.5-11.1 μm^3/voxel were used.

The sample was oriented in the positive *x, y, z* position and firmly affixed to the rotating table using hot-melt glue. To minimize beam hardening and ring artefacts, a 5mm thick copper filter was used between the X-ray beam source and the sample. Table 3-2 summarizes the settings, resolutions, and size of each scan.

The datos|x acquisition software system was used to calibrate the images prior to data acquisition. The calibration required a pixel correction mask to minimize hotspots on the detector. Once the image data was collected, the datos|x software was used to reconstruct the microCT scanned images.

The microCT data was processed in three main stages: a) cropping, b) filtering, and c) binary thresholding. These main processing steps are outlined in two-dimensions in Figure 3-1. The microCT image stacks were cropped to remove any voxels that exhibited edge effects, such as beam hardening, or material removal from the use of a dremel tool to cut the samples. Beam hardening occurs at the limit of the material due to the change in density from material to vacuum [62, 63, 112]. The *x,y,z* dimensions of the cropped samples are summarized in Table 3-2. The cropped image stacks were filtered using a hybrid three-dimensional median filter to remove residual noise [20, 116].

The cropped microCT image stacks were filtered using a hybrid three-dimensional median filter on a 4^3 voxel subvolume, the smallest possible subvolume, similar to the filtering conducted by Ji et al. [20]. The three-dimensional median filter with centre-pointing was used to reduce voxel noise and enhance the pore edges [48, 49]. In a median filter with centre-pointing, the median gray value of the subvolume is applied to the centre voxel of each subvolume instead of being applied to the full subvolume. Filtering was performed using the hybrid three-dimensional median filter plugin [117] for Fiji/ImageJ [118].

The three-dimensional median filter reduced the pore surface roughness while maintaining the pore volume and removed random noise [116]. The noise within the microCT data can originate from defects in the detector and impurities within the copper filter [119]. In this study, three-dimensional median filtering was required because when the Indiana Limestone samples were extracted without filtering, the pore space contained many single-voxel pores and low connectivity, which were unphysical. As well, the pore

network of unfiltered Pink Dolomite samples could not be extracted in a feasible timeframe. Following three-dimensional median filtering, the cropped and filtered microCT image stacks were converted to binary image stacks.

To determine the pore space from the three-dimensional greyscale images, they must be converted to black-and-white images. Otsu's method [71] was applied to the entire three-dimensional image stack to separate the void and material space into two distinct regions. Otsu's method [71] determines a single threshold value (black and white cutoff) based on a minimization of the variance between the greyscale value of the voxels above and below the evaluated threshold. The grayscale threshold is recursively searched from the histogram values by minimizing the spread (also called variance) of the distributions above and below the threshold. Otsu's method [71] was selected as the thresholding algorithm because it provided a threshold based directly from the greyscale histogram of the microCT image data. As well, Otsu's method thresholds three dimensional microCT image data. The conversion of the image into its pore space and material is a critical stage [20, 67, 74, 75], since an incorrect segmentation can lead to over- or under-estimation of the pore space. Further discussion on selecting an appropriate threshold technique is included in Chapter 4.

3.2.3 Pore Network Extraction and Invasion Percolation

The segmented microCT data was resolved into a binary representation of the pore and material space, which was then used as input to the pore network extraction algorithm. Pore network extraction converts the imaged pore space into a simplified geometric representation by storing only the locations of spherical pores connected by cylindrical throats. The pore network was extracted from the processed image stack using a modified watershed algorithm [98]. From the extracted pore network, statistical parameters (pore size, pore radius, throat radius, pore coordination number, and pore-to-pore distance) describing the geological core samples were determined.

The pore network extraction was used to determine the pore space, pore size distributions and pore geometry. The samples presented here contained between 91 and 198 million voxels. To determine the saturation-capillary pressure relationship of the core samples studied, invasion percolation simulations were required. Invasion percolation simulations

were performed on each extracted network using modeling software developed by Hinebaugh et al. [98] to determine the breakthrough saturation and capillary pressure vs. volume saturation curves.

3.3   Results and Discussion

Pore network modeling was conducted on microCT data of Indiana Limestone and Pink Dolomite to determine their microstructure and assess their suitability as target formations for carbon dioxide sequestration. A high-throughput method for extracting the pore space of Indiana Limestone and Pink Dolomite from reconstructed three-dimensional images was established. The pore space provides input geometries for microscale flow studies of core scale properties and input parameters for reservoir scale investigations.

The following results include the mineral compositions of the carbonates, the pore scale geometric properties, and their comparison to literature values [30, 31, 67]. These results provide a dataset of geometric parameters for use in future upscaling simulation studies.

The bulk mineral composition of Indiana Limestone and Pink Dolomite were determined using X-ray fluorescence spectroscopy as 98.6% and 99.4% calcite ($CaCO_3$) by weight percent, respectively. The mineral composition of the Indiana Limestone matched that reported in the Indiana Limestone Handbook for bulk mineral composition [56]. The mineral composition of Pink Dolomite was not reported in literature. Table 3-3 shows the complete chemical composition of the rocks, as found using X-ray fluorescence spectroscopy. Since both rocks were primarily calcite (Table 3-3), a single contact angle could be used in the invasion percolation studies [57].

The pore geometry of Indiana Limestone and Pink Dolomite were analyzed. The statistical distributions that were determined include the mean pore volume radius, mean pore radius, mean throat radius, the pore coordination number, and the pore-to-pore distance, and each will be compared and discussed below. In all cases, the geometric properties reported are the mean of all the samples, and the associated standard deviation. Figure 3-2 shows sample slices of the microCT imaging for (a) Indiana Limestone and (b) Pink Dolomite which were extracted to pore network models to determine the geometrical parameters of the samples.

3.3.1   Porosity

The porosity for the Indiana Limestone samples was determined to be (12±2) %. The measured porosity (12±2) % is lower than the sample provider's reported porosity of 19%. This was likely due to the presence of micropores below the resolution of the microCT. Microporosity is discussed in Chapter 4. Since the porosity of the investigated Indiana Limestone samples matched that reported by other researchers [30, 67], this showed the image processing and segmentation technique employed in this study was able to capture the macroporosity of Indiana Limestone samples.

The porosity of the Pink Dolomite samples was determined to be (26±9) %. The porosity has a large standard deviation compared to the Indiana Limestone samples, which was due to pore and material features present in two of the Pink Dolomite samples (Figure 3-3 b and c). In (b), a large pore (circle), also called a vug, resulted in a higher porosity and in (c), a region with high material fraction (box) led to a lower porosity. If the second and the third samples are not included, the mean porosity of the Pink Dolomite samples is (27±2) %. The Pink Dolomite samples exhibited much less heterogeneity of the pore space compared to Indiana Limestone, as shown in the SEM images in Figure 3-2 (c) and (d). A higher porosity signifies a larger void volume, and therefore a larger amount of carbon dioxide that can be stored in a given volume of rock.

In the following sections, the statistical distributions describing the pore geometry are presented. These include the pore size, pore radius, throat radius, pore coordination number and pore-to-pore distance. The Indiana Limestone pore space statistics were validated against literature values, and are found in Table 3-4. The pore size distributions were fit to lognormal distributions to demonstrate that the geometric properties discussed can be used as inputs to micro flow simulations, which require descriptions of the bulk pore space.

3.3.2   Pore Size

The pore size distributions for the Indiana Limestone and Pink Dolomite extractions are shown in Figure 3-4. Knowledge of the pore size distributions is important when modeling or determining the permeability and overall capacity of the core samples [29]. The Indiana Limestone samples have a larger variance, while the pore sizes for Pink

Dolomite are more concentrated near the mean. Figure 3-4 shows representative distributions for both rock types. The distributions for the other samples were similar.

Indiana Limestone samples had a mean pore size of $(20\pm3)\mathrm{x}10^3$ μm^3. The Pink Dolomite samples had a mean pore volume of $(7.3\pm0.2)\mathrm{x}10^3$ μm^3. The Indiana Limestone samples were similar to one another, represented by a standard deviation of 3%. Representative lognormal fits to the pore size distributions are shown in Figure 3-5, along with the mean and variance that describe the distributions. The variance of a lognormal fit is a measure of how the values scatter around the mean. A larger variance indicates the values scattered more around the mean, and the mean is therefore less representative of the overall sample set. The fits were determined using DFitTool in Matlab. The variance of the Pink Dolomite lognormal fit was 70% lower than that of the Indiana Limestone, which indicates the Pink Dolomite samples were more homogeneous in their pore sizes than the Indiana Limestone samples. In general, a larger mean pore size can indicate a higher permeability and a preferred material for carbon dioxide injection dependent on the overall connectivity of the pores.

3.3.3 Pore Radius

Representative pore radius distributions of the samples, as shown in Figure 3-6, were determined using the pore network extraction algorithm [98]. For both rock types, pore radii are in the range of 10-100 μm. Only one sample of each rock type are shown in Figure 3-6 for Indiana Limestone and Pink Dolomite as they were representative of the four Indiana Limestone and Pink Dolomite samples (Table 3-4). The mean pore radius of Indiana Limestone was determined to be (31 ± 2) μm, with the standard deviation representing up to a 6.5% deviation from the mean.

When the pore radii for the Indiana Limestone samples were compared to other studies [30, 67], the technique used here found values three times larger. One possible explanation for this deviation lies in the definition of a pore used by those authors. In the work of [30, 67], a pore is defined as the maximum circle inscribed within a triangle, and a throat as the connection between the pores [103]. Their definition of a pore led to a higher number of throats than pores due to an inverse correlation between the pores and throats, whereas the pore network model employed here, after the development by

Hinebaugh et al. [98], led to a higher number of pores than throats. Zhu et al. [31] performed an analysis of Indiana Limestone and found pore radii in the range (25-50) µm, which compares well with the results from this analysis, r_{pore} = (31±2)µm. The agreement between the thin-section analysis method [31] and the pore network extraction used in this study demonstrates that the pore network method can capture physical rock pore spaces.

The mean pore radius of the Pink Dolomite pore space was determined to be r_{pore} = (21±1) µm. The standard deviation represented 5% of the total mean radius, which demonstrates little variability within the Pink Dolomite samples. Similar to the pore volume distribution, the standard deviation of the mean pore radius was larger for the Indiana Limestone samples than for the Pink Dolomite samples. A larger mean pore radius indicates a higher permeability, which is preferred for materials that will be injected with carbon dioxide. The pores that had a radius of a single voxel for both Indiana Limestone and Pink Dolomite were exclusively unconnected and represented between (30-50) % of all pores. This was due to the lower spatial resolution of the microCT data, whereby pores with radii less than a single voxel length could not be resolved.

The pore radii distributions for Indiana Limestone are comparable to literature values [31]. The Pink Dolomite pore radii distributions are the first reports of this rock, to the author's knowledge. For both rock types, the pore radii distributions determined here can be used to develop simulated pore networks comprising a larger volume than those investigated in this study.

3.3.4   Throat Radius

The mean throat radius of Indiana Limestone was determined to be (22±1) µm. The standard deviation associated with the throat radius represented 4.5% of the mean. The mean throat radius for Pink Dolomite was (13.6±0.4) µm. The associated standard deviation is 3% of the mean throat radius, representing little variation between the Pink Dolomite samples compared to the Indiana Limestone samples. However, it must be noted that the reported mean throat radius is approximately two times the resolution of the Pink Dolomite samples. Hence, the spatial resolution plays a role in the throat radius that

can be resolved from the microCT. In general a larger throat radius indicates a higher permeability and a preferred material for carbon dioxide injection.

3.3.5   Pore Coordination number

The pore coordination number distributions of Indiana Limestone and Pink Dolomite, seen in Figure 3-7, show a consistent range from a coordination number of 1 to 20. The mean pore coordination number of Indiana Limestone was determined to be (2.6±0.2), which is similar to the literature value of 2.97 in [30, 67]. As discussed in Section 3.3.3, the deviation between Gharbi et al. [67], and this study (approximately 14%) is likely due to the different pore network models employed here and in those studies. Despite these variations, the majority of the pore space geometry statistics are comparable, see Table 3-5. As well, those authors do not report the full distribution of the coordination number; this information provides other researchers an additional level of detail for larger scale pore network simulations of limestones and dolomites.

The Indiana Limestone mean coordination number had a standard deviation of 8%. This implies that, in spite of the variability between the pore space geometry, the pore coordination is consistent between the samples. For the Pink Dolomite, the mean coordination number was determined to be (1.9±0.1), with a 5% standard deviation from the mean. The actual range of the coordination for Pink Dolomite, from 1 to 30, was larger than Indiana Limestone, which ranged from 1 to 20.

The Indiana Limestone and Pink Dolomite coordination number distributions, seen in Figure 3-7 , were both log-normal distributions. The mean pore coordination number was similar for the Pink Dolomite and Indiana Limestone samples, and both exhibited higher mean coordination numbers than other carbonates investigated by Gharbi et al. [67]. A higher coordination number implies better connectivity of the pore space, and therefore a suitable carbonate for injection of carbon dioxide. The coordination number distributions can be used to develop simulated networks for use in pore transport modeling studies.

3.3.6   Pore-to-Pore Distance

The pore-to-pore distance for Indiana Limestone was (137±8) μm. The standard deviation of the mean is small, meaning there was little variation between the samples

investigated. For Pink Dolomite, the pore-to-pore distance was (95±7) μm, shorter by 44% than the Indiana Limestone. However, as seen in the SEM images in Figure 3-2, this result is expected by a visual qualitative comparison of the mean pore-to-pore separation. A higher pore-to-pore distance implies a lower permeability and a less suitable carbonate for carbon dioxide injection due to the larger paths the flow would need to traverse in order to fill the nearest pore.

3.3.7   Invasion Percolation Simulations

The throat diameter vs. volume saturation curves for sample 1 of Indiana Limestone and Pink Dolomite, see Figure 3-8, show the behavior of the pore network over a range of throat diameters. Using the Washburn equation (Equation 2.3) the pressure can be interchanged with the throat diameter. To interpret Figure 3-8, once the pressure was sufficient to enter a given throat diameter, the volume could be saturated to the corresponding fraction. Indiana Limestone was slightly less permeable than Pink Dolomite, while both had similar breakthrough saturations as a fraction of their respective total pore volumes. The breakthrough saturation is determined as the highest saturation value on the capillary pressure vs. volume saturation curves. The Indiana Limestone curve (in dashed dark grey) has a value of 45%, while the Pink Dolomite curve (in grey) has a value of 55% saturation. The mean saturation of Indiana Limestone and Pink Dolomite for the samples investigated were (48±4) % and (50±5) %, respectively. This indicates that both rocks have a substantial fraction of their pore volume accessible for injected carbon dioxide. A higher saturation is generally desirable, as it means that a larger proportion of the rock is available, and accessible for injected carbon dioxide.

3.4   Conclusions

The objective of this study was to characterize the microstructure of the model limestone and dolomite cores, and to begin to assess the transport parameters describing the flow through these materials. The statistical distributions of the pore geometry were successfully determined for Indiana Limestone and Pink Dolomite, as structural input parameters for pore scale and reservoir scale simulations of carbon dioxide injection into saline brine-filled porous rock structures to estimate the carbon dioxide storage capacities of these formations. The distributions were found using a pore space extraction scheme

based on the Watershed algorithm, which has seen limited application in pore network modeling of geological structures, in spite of its computational efficiency and ability to handle large data sets.

The key statistical characteristics of the pore space determined for Indiana Limestone and Pink Dolomite include: mean pore volume, mean pore radius, mean throat radius, mean coordination number, and mean pore-to-pore distance. The statistical pore space distributions showed good agreement with literature values for Indiana Limestone. The porosity was within 8% of the literature values of Gharbi et al. [67] and Bijeljic et al. [30]. The pore radius was within 21% of the mean pore radius determined by Zhu et al. [31]. The coordination number was within 14% of the coordination number determined by Gharbi et al. [67]. This work presents the first pore scale description of Pink Dolomite, as there is little discussion in literature on this carbonate. These statistical distributions can be used in future studies as inputs to pore scale and reservoir scale simulations of underground fluid transport.

The groundwork to evaluate the transport parameters of permeability and tortuosity were laid through a first assessment of the saturation profiles of Indiana Limestone and Pink Dolomite and the extraction of the microstructure properties.

3.5 Tables

Table 3-1: Summary of the core properties obtained from Kocurek Industries

Geologic Material	Supplier	Formation and Location	Brine Permeability (milli-Darcy)	Gas Permeability (milli-Darcy)	Porosity (%)
Indiana Limestone	Kocurek Inc.	Bedford, Indiana, USA	70	200	19
Pink Dolomite	Kocurek Inc.	Edwards Plateau, Texas, USA	50	94	29

Table 3-2: Summary of the sample sizes, voxel resolutions and dimensions

| | Sample | Approx. Dimensions (mm) | | Voltage (kV) | Current (μA) | Voxel Resolution (μm) |
		Cylinder, before cropping (diameter, height)	Block, after cropping			
	#1	6, 8.5	4.4 x 3.6 x 7.7	120	90	11.07
Indiana	#2	6, 6.5	3.6 x 4.3 x 5.0	135	60	8.3
Limestone	#3	6, 9.0	3.3 x 3.0 x 6.6	135	60	8.3
	#4	6, 8.5	3.8 x 3.9 x 5.8	135	60	8.3
	#1	6, 8.5	4.5 x 3.7 x 6.0	120	60	8.3
Pink	#2	6, 8.0	4.2 x 3.8 x 5.3	120	60	7.5
Dolomite	#3	6, 9.0	3.7 x 3.5 x 6.3	120	60	7.5
	#4	6,7.0	3.4 x 3.5 x 4.5	120	60	7.5

Table 3-3: X-ray fluorescence results for Indiana Limestone and Pink Dolomite.

Indiana Limestone		Pink Dolomite	
Chemical Compound	Atomic Weight (%)	Chemical Compound	Atomic Weight (%)
$CaCO_3$	98.577	$CaCO_3$	99.391
MgO	0.560	K_2O	0.140
SiO_2	0.352	MgO	0.136
FeO	0.143	Cl	0.104
Al_2O_3	0.117	SiO_2	0.091
K_2O	0.077	FeO	0.070
Cl	0.064	Al_2O_3	0.034
S	0.048	Sr	0.016
Na_2O	0.031	S	0.012
Sr	0.021	P_2O_5	0.007
P_2O_5	0.010	—	—

Table 3-4: Pore structure parameters determined for Indiana Limestone and Pink Dolomite

Pore Structure Characterization	Indiana Limestone	Pink Dolomite
Porosity (%)	(12±2)	(26±9)
Mean Pore Size (μm^3)	(20±3)x10^3	(7.3±0.2)x10^3
Mean Pore radius (μm)	(31±2)	(21±2)
Mean Throat radius (μm)	(22±1)	(13.6±0.4)
Mean Pore Coordination number	(2.6±0.2)	(1.9±0.1)
Mean Pore-to-Pore Distance (μm)	(137±8)	(95±7)

Table 3-5: Statistical measures of the pore space of Indiana Limestone compared to the
measures determined by Gharbi et al. [67] and Bijeljic et al. [30]

Statistical Measure	Indiana Limestone	Indiana Limestone, Gharbi et al. [67]	Indiana Limestone, Bijeljic et al. [30]
# of Samples	4	1	1
Porosity (%)	(12±2)	13.05	11
Number of voxels	~450^3-530^3	330^3	330^3
Voxel Resolution (μm)	8.3,11.1	7.7	7.7
Physical sample volume after cropping (mm^3)	66.5-123.4	16.41	—
Mean Pore Size (μm^3)	(20±3)x10^3	—	—
Mean Pore Radius (μm)	(22±1)	10.17	10.17
Mean Pore Coordination Number	(2.6±0.2)	2.97	2.97
Number of Pores (#Pores)	9615-17960	5653	—
Number of Throats (#Throats)	5603-11879	8539	—

3.6   Figures
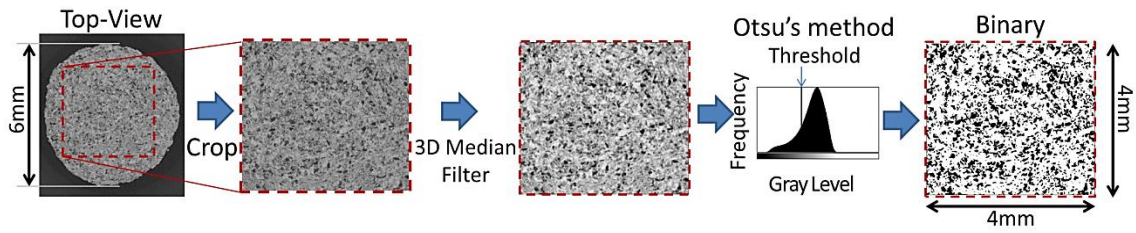
Figure 3-1: Schematic for a Pink Dolomite sample on how the rock samples were
processed, and converted to binary images using a single Otsu threshold.
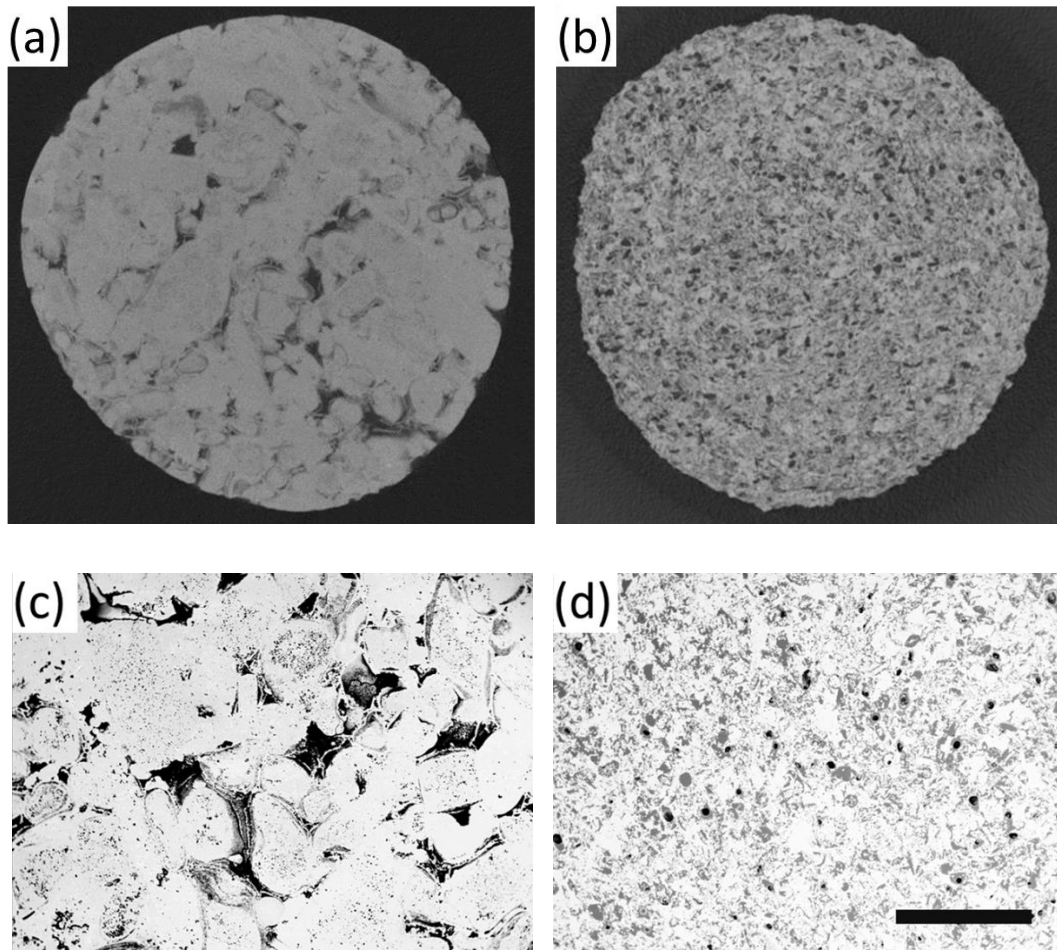
Figure 3-2: MicroCT data cross-section of Indiana Limestone (a); and Pink Dolomite (b) at 8.3μm and 7.5μm resolution, respectively. The diameter of the cores in (a) and (b) are approximately 6mm. SEM images of (c) Indiana Limestone and (d) Pink Dolomite show the microporosity and heterogeneity of the samples. The length bar is applicable to (c) and (d) and represents 1 mm.
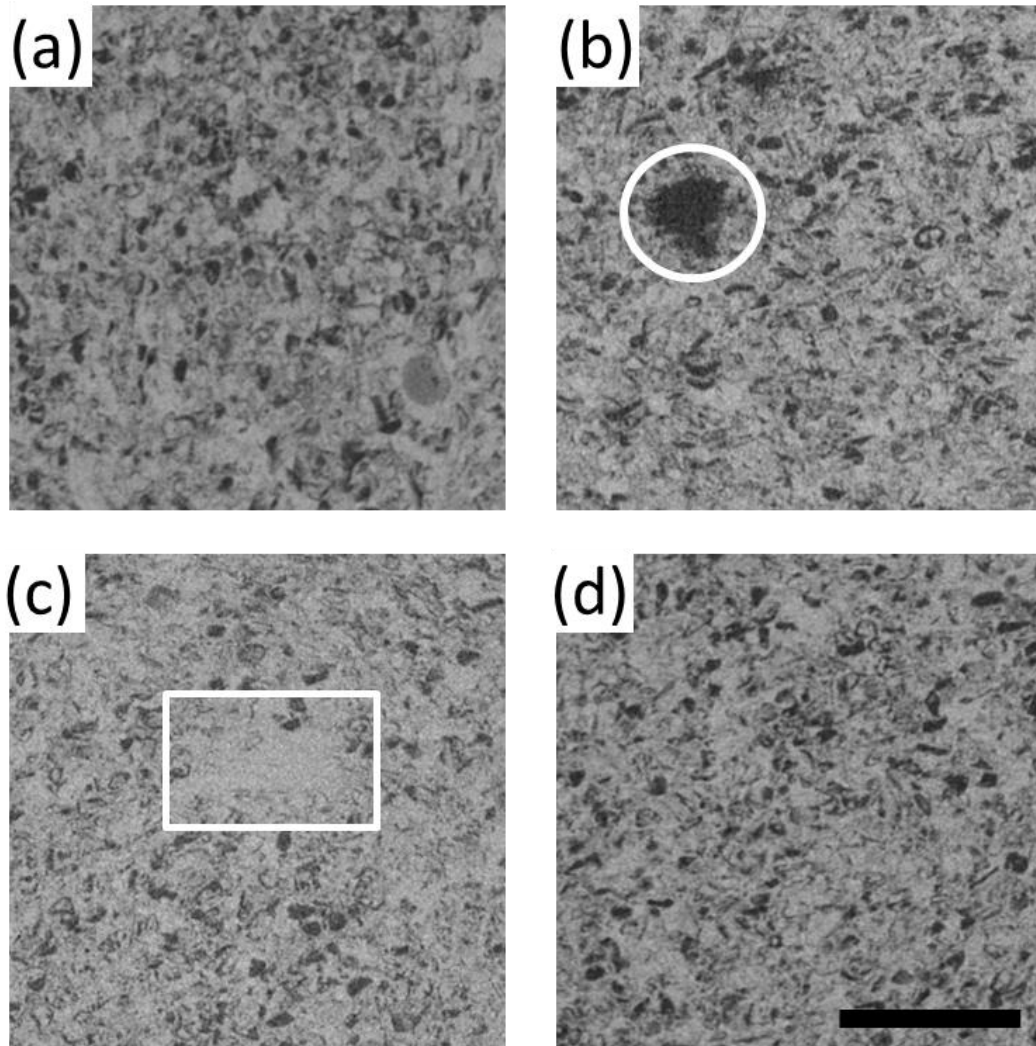
Figure 3-3: Greyscale slices of the microCT image stacks show significant differences among the Pink Dolomite samples. Figures (a)-(d) are the Pink Dolomite samples 1-4, respectively. In (b) the large pore, also called a vug is circled in white. In Figure (c) the solid material region is highlighted with a white rectangle. The length bar is applicable to (a) - (d) and represents 1 mm.
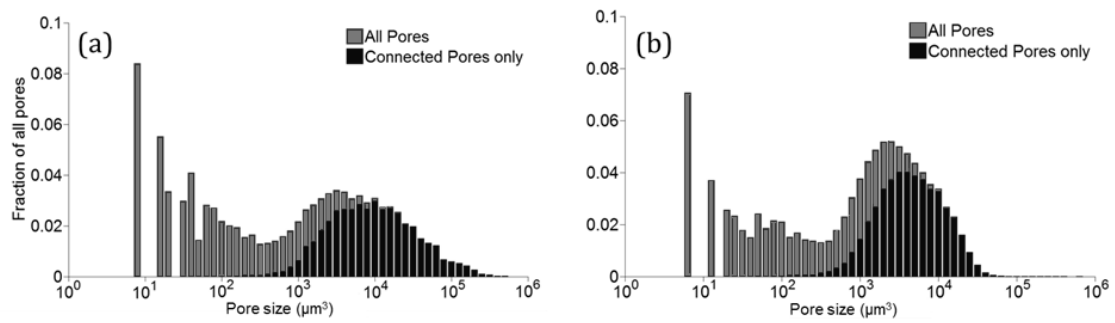
Figure 3-4: Indiana Limestone (a) and Pink Dolomite (b) distributions of the pore size.
Grey signifies all pores, and black represents the connected pores only.
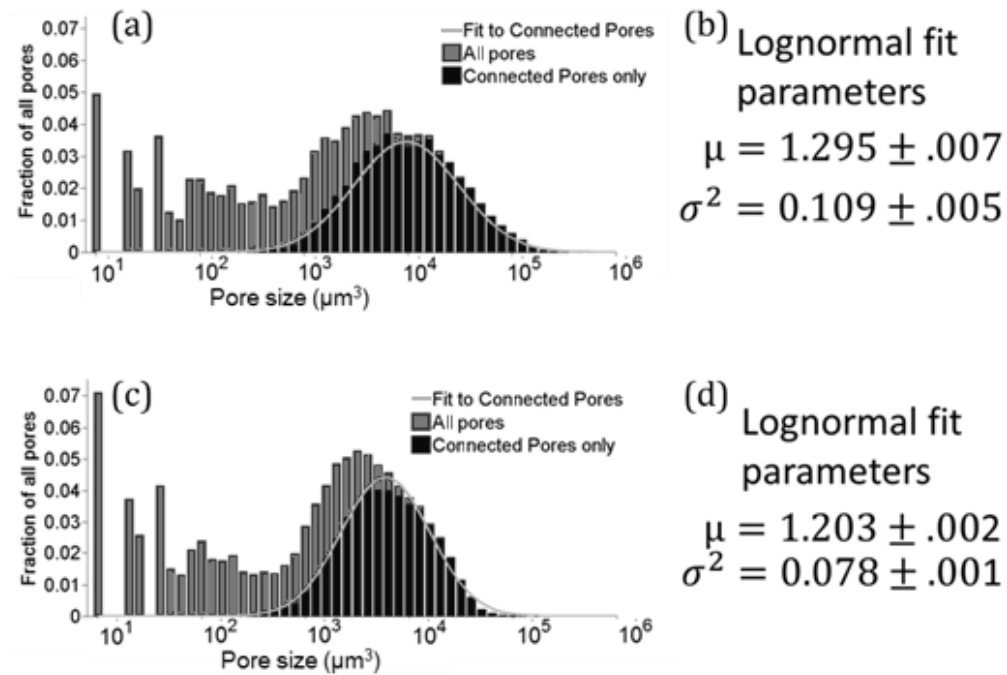
Figure 3-5: Pore size distributions for (a) Indiana Limestone, and (b) the associated lognormal fit to the distributions. Pore size distribution for (c) Pink Dolomite with (d) the associated lognormal fit to the distributions. Note that the means and variances reported here are for the lognormal distribution.
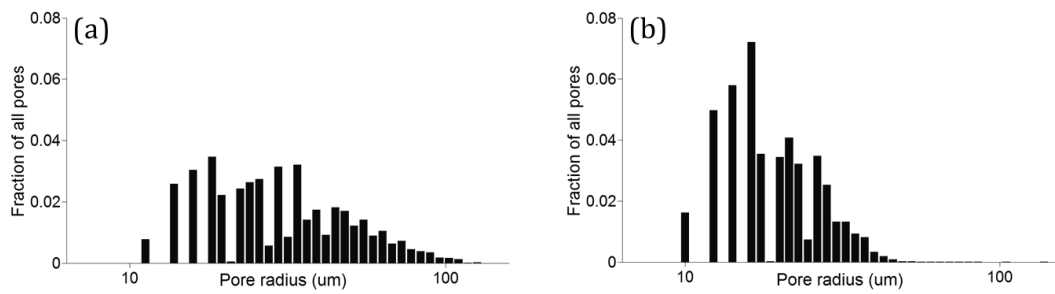
Figure 3-6: Pore radius distributions of the connected pores of the Indiana Limestone (a) and Pink Dolomite (b) samples.
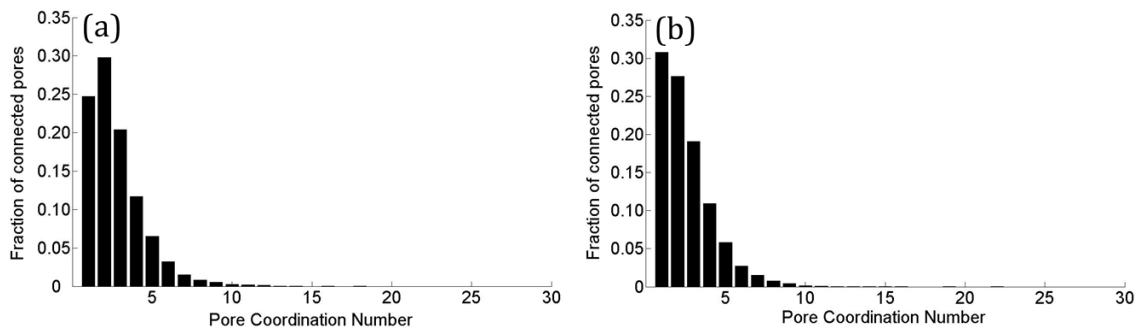
Figure 3-7: Pore coordination number distributions for the Indiana Limestone (a) and Pink Dolomite (b) samples.
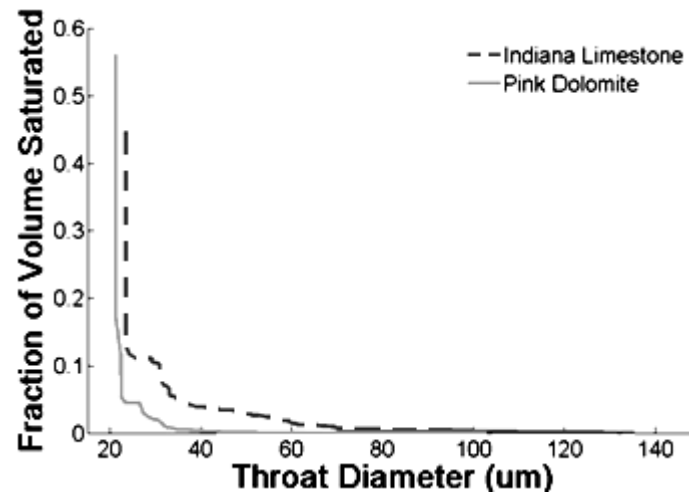
Figure 3-8: Invasion percolation simulation results for Indiana Limestone (in dashed black) and Pink Dolomite (in grey).

Chapter 4
Dual Porosity of Indiana Limestone and Pink Dolomite

4.1   Introduction

Carbon dioxide (CO_2) sequestration in underground geologic reservoirs is recognized as a viable technology, which has the potential of reducing atmospheric greenhouse gas emissions [1]. In geologic carbon sequestration, CO_2 resulting from fossil fuel–based electricity generation or oil sands processing, for example, is injected into a suitable high-permeability deep geologic formation to fill the rock pore space. The CO_2 is prevented from returning to the atmosphere by sealing the formation with a low-permeability cap-rock. Part of the evaluation process to determine the suitability of potential storage reservoirs involves estimating the CO_2 storage capacity [114] of the bedrock. This can be determined from knowledge of reservoir transport properties, including permeability and connectivity [10]. In particular, an accurate measure of the reservoir porosity is required to estimate the local transport properties that are used as inputs to reservoir scale simulations.

These transport properties have been well-characterized for conventional oil-bearing formations such as sandstone, both from earlier work in the petroleum industry [6, 7] and advances in carbon capture and storage [16, 120, 121]. Carbonate rock reservoirs have attracted recent attention within the carbon capture and storage industry, due to their abundance in the earth's crust, as potential CO_2 storage sites [11, 12]. However, due to the spatial heterogeneity inherent in carbonate rock formations, and the associated difficulty in obtaining accurate global porosity measurements, the determination of a carbonate rock reservoir's CO_2 storage capacity remains a challenge [2].

Advances in X-ray micro-computed tomography (microCT) have enabled the evaluation of the transport properties of sandstones by providing a three-dimensional image of the rock's internal pore space [66, 122, 123]. In addition, microCT imaging has allowed the development of suitable upscaling techniques, such as adapted local-global averaging [124], which provide macroscale transport properties for reservoir simulation as derived

from detailed volumetric core sample images obtained from rock core samples [50, 125, 126]. Some of the benefits of this technique include the determination of local-core scaled flow and geochemical transport parameters, including local porosity, permeability, and species transport models directly from microCT data instead of from large-scale field measurements [17, 21, 22]. Deriving relationships between porosity and flow-based properties for carbonate reservoirs remains an area of active research, due mainly to the complexity of carbonate structures because of their dual porosity [21-31]. Dual porosity refers to a void volume with porous features across multiple length scales. It is characterized by both an apparent macroporosity, having features well above the spatial resolution of microCT imaging, and a microporosity with porous features near or below the microCT resolution. As a result, the estimation of transport properties such as permeability and tortuosity, is more challenging than for single porosity rocks since correlations, such as Archie's Law, are no longer applicable [76]. Further, characterizing the dual porosity is in itself a challenge, since the pore sizes range from nanometers [66] to centimeters [77]. A single imaging technique cannot visualize pore sizes across disparate length scales, so the use of multiple imaging techniques is required [36, 37].

Experimental techniques used to measure the local pore structure of geological materials include thin-sectioning [57], microCT [62, 63, 112], and backscattered electron scanning electron microscopy (SEM) [38, 42]. These techniques are introduced subsequently. Thin-sectioning analysis involves optical microscopy of thin cross-sections of rock samples, and the subsequent combination of the individual images into a volumetric representation [57]. This technique is limited by the low resolution capabilities of light microscopy and by how thin rock core sections can be sliced. Micro-computed tomography is a non-destructive technique for volumetric characterization of porous materials [62, 63, 112]. Because it is non-destructive, measurements performed with microCT can be repeated on the same material. Since the samples remain intact, other analyses such as SEM and chemical composition can be performed on the same samples analyzed by microCT. The three-dimensional volume image provided by microCT is recorded as a series of images, called an image stack. Micro-computed tomography can achieve spatial resolutions up to 1 μm/voxel. A voxel is a three-dimensional pixel, while the pixel is the smallest unit of a two-dimensional image. For higher spatial resolutions, scanning electron microscopy can

be conducted to achieve spatial resolutions up to 1 nm/pixel [57]. Scanning electron microscopy involves the two-dimensional imaging of a cut rock surface using a high-energy electron beam [58]. This technique can provide a highly accurate determination of the local porosity, but it is limited to a two-dimensional plane, and only a limited number of images can be obtained, due to the time required to generate a single image.

For microCT and SEM, the output is a digital image where each voxel (in the case of microCT) or pixel (in the case of SEM) is assigned a grayscale value. When the area or volume being imaged exhibits features below the resolution, the grayscale value represents an average of the relative amounts of void and material across each digitized area. This effect presents particular challenges for microCT, due to its lower resolution. In spite of this, microCT has been the preferred method for characterizing the pore space, since it provides three-dimensional volumetric imaging data of the pore space [62].

The accurate determination of local porosity from two- or three-dimensional imaging data requires the conversion of the images into solid and void space. This entails the segmentation of the grayscale images into binary (black and white) data, which involves the determination of a threshold greyscale value. A threshold is defined as the greyscale value above which all the pixels or voxels are assumed to be solid material (white), and those below are treated as void (black). The technique used to find an appropriate threshold value depends on the type of material being segmented and the pore structure of that material. For porous materials that have a uniform pore size, such as sandstones, or materials with a high-contrast between the material and the pore space, the segmentation is a straightforward process. However, for dual porosity rocks such as carbonates it is challenging to capture the full range of the pore structure features with a single imaging technique [19-21]. Therefore, more advanced thresholding methods are required.

Thresholding techniques are categorized in the literature as local or global [91, 129]. Local thresholding techniques depend on the spatial variation of the greyscale values [130]. Global thresholding techniques rely on the greyscale histogram of the entire image, and are therefore more suitable for three-dimensional volumes [91]. A review of thresholding techniques has been compiled by Sezgin et al. [131].

A common global thresholding technique for sandstones and carbonates is Otsu's method [20, 30, 67, 72-74]. In Otsu's method, the greyscale value that minimizes the variance between the black pixels (void), and white pixels (solid) is designated as the threshold. However, Otsu's method often underestimates the porosity of carbonates with dual porosity, such as Indiana Limestone [20]. This is because it does not account for the porous features below the spatial resolution of the imaging method. The pores below the resolution of the imaging method are defined as micropores, and the associated porosity is called microporosity. While the pores above the resolution of the imaging method are defined as macropores, and the associated porosity is called macroporosity. To overcome this limitation, Ji et al. [20] , Bauer et al. [29] and Galaup et al. [21] have introduced new techniques to quantify the dual porosity of carbonates. Galaup et al. [21] performed experimental measurements using SEM on samples intruded with woods metal to quantify the microporosity of carbonates and dolomites. Bauer et al. [29] developed a dual pore network model to account for the dual porosity of carbonates by segmenting the grayscale histogram from microCT data into three regions: solid, microporous and macroporous using the intersection of three Gaussian distributions to provide two thresholds. Ji et al. [20] improved upon the segmentation in [29] by using Otsu's method directly on the grayscale histogram to determine the two thresholds and divide the grayscale histogram into three regions. Ji et al.'s [20] technique removed the fitting of three Gaussian distributions to the data, since not all dual porosity grayscale histograms exhibit three Gaussian distributions [20]. Although each of these techniques were developed and applied, the literature lacks a thorough comparison of available techniques as a first step towards developing a systematic methodology for analyzing dual porosity materials.

The objective of this chapter is to provide a comparison of thresholding techniques of SEM and microCT data as applied to Indiana Limestone and Pink Dolomite. Although SEM can be conducted at high resolution the data lack information on the three-dimensional pore space of the rocks. The microCT data provides a three-dimensional representation of the pore space, which is necessary to perform pore network modeling and pore space analyses.

4.2   Methods

In this study, three techniques for measuring the porosity of carbonates was applied to SEM and microCT data of Indiana Limestone and Pink Dolomite as a comparison of the measured porosities. The first technique assessed was single Otsu's method [71], the second technique was that of Ji et al. [20], the third technique involved the porosity determined from thresholding high resolution SEM images.

In single Otsu's method [71], the grayscale histogram is divided into two regions, black and white separated by a threshold. The single threshold is determined by minimizing the spread (also called variance) between the greyscale value of the voxels above and below the evaluated threshold. The grayscale threshold is recursively searched in the histogram by minimizing the variance of the distributions above and below the threshold.

In the greyscale histogram of dual porosity materials, two distributions are present which tend to be Gaussian [20, 29]. To determine the total porosity, Ji et al. [20] performed a series of thresholds on the full three-dimensional bimodal greyscale histogram. The first peak in their data represented the mode of the void space (I_{void}) and the second, the solid space (I_{solid}). Then they performed Otsu's threshold once on the full histogram to determine the first threshold Ji_1. Then they performed Otsu's method a second time on the histogram above Ji_1 to determine the second threshold Ji_2. Both Ji_1 and Ji_2 are located in the region between the peaks of the two Gaussian distributions (I_{void} and I_{solid}), as shown in Figure 4-1. Between Ji_1 and Ji_2, the microporosity (φ_{local}) was derived using the following relation:

$$\varphi_{local} = \frac{I_{solid} - G}{I_{solid} - I_{void}} \qquad (4.1)$$

where G is the greyscale value being evaluated, I_{solid} is the grayscale value of the peak of the solid region, and I_{void} is the peak of the void region. A weighted summation is then applied to the greyscale frequencies to determine the contribution of the microporous region to the total porosity.

The two thresholding techniques for microCT data (single Otsu and Ji et al. [20]) were then compared to the porosity determined from SEM image data.

4.3 Experimental Methodology

In this section, the carbonate samples investigated are presented, the sample preparation and imaging methodologies are described, and the image processing techniques used are outlined.

The geologic materials investigated were Indiana Limestone and Pink Dolomite. Four samples of each were studied using microCT. A single sample each of Indiana Limestone and Pink Dolomite were randomly selected for analysis with SEM. As this was a preliminary comparison of techniques a single sample of each carbonate was chosen to perform SEM.

4.3.1 MicroCT Sample Preparation and Imaging Technique

The microCT data was processed in two primary stages. First, the microCT image stacks were cropped to remove edge effects due to beam hardening and material removal from the preparation of the sample by cutting. Beam hardening occurs at the limit of the material due to the X-ray beam traveling through an abrupt change in density from material to vacuum [62, 63, 112]. Second, the image stack was segmented into binary volumetric data using two thresholding techniques: single Otsu, and Ji et al.'s [20] dual Otsu threshold. Each technique was compared for its measured porosity.

4.3.2 SEM Sample Preparation and Image Processing Technique

The rock samples were analyzed using a JEOL JSM6610-Lv Scanning Electron Microscope (JEOL Ltd., Tokyo, Japan). The machine was equipped with an Oxford solid state energy dispersive system with an ultra-thin window and was operated at the Geology Department of the University of Toronto. The samples were epoxy-impregnated prior to polishing. Polishing of the sample was conducted with a fine grain diamond polisher. Then, the polished sample was sputter-coated with a 200 nm layer of gold in preparation for SEM imaging. The gold layer provided a conductive layer for the electron beam during imaging [132].

The recorded SEM greyscale images were then cropped to remove blurring effects (from the refraction of the electron beam through the lens) at the edges. The cropped images were then converted to binary images using each of twelve global thresholding techniques within Fiji image processing software [118]. The techniques which were determined of these twelve to be the most relevant were selected based on an evaluation of thresholding methods by Sezgin et al. [133]. For Indiana Limestone, the top four ranked global thresholding methods by Sezgin et al. [133] applicable to a single peak histogram were used to determine the mean total porosity. These were: Minimum Error [134], Maximum Entropy [135], Renyi Entropy [136], and Yen [137]. For Pink Dolomite, the two thresholding techniques which were applicable to bimodal histograms were used to determine the mean total porosity. These were: Intermodes [138] and Minimum [138]. The total porosity, including the microporosity, was then used as a comparison to the porosity determined using the single Otsu and Ji et al.'s [20] dual Otsu threshold technique.

4.4   Results and Discussion

In this section, the results of the thresholding procedures performed on the microCT data, shown in Figure 4-3, are first presented for Indiana Limestone and then compared to the total porosity observed in the SEM images. The SEM images are shown in Figure 4-4, where the very high resolution SEM images show that the microporosities of both the Indiana Limestone and the Pink Dolomite were below the resolution of the microCT data. Second, the results are presented and discussed for Pink Dolomite. Finally, a comparison between the results of Indiana Limestone and Pink Dolomite is presented.

4.4.1   Indiana Limestone

The four Indiana Limestone samples and their microCT grayscale histograms were analyzed to determine the total porosity, including the microporosity, using the two binary thresholding techniques: single Otsu, and Ji et al. [20]'s dual Otsu. A representative greyscale histogram showing the various threshold locations is shown in Figure 4-1 (a). The single Otsu threshold determined the total porosity to be (13 ± 1) %, while for Ji et al.'s [20] dual Otsu thresholding technique, it was determined to be (14 ± 5) %. The results of the microCT methods were then compared to the porosity

determined using high spatial resolution (1.5 μm/pixel) SEM images. The SEM images serve as a high resolution measure of the porosity. To obtain a measure of the total porosity, however, the greyscale SEM images must be thresholded. There is significant variation in porosity between the various thresholding techniques, as seen in Figure 4-5. The top four ranked techniques by Sezgin et al. [131] were used to determine the mean threshold value and porosity and were applied to the greyscale histogram (Figure 4-6 (a)). The greyscale histogram of Indiana Limestone shows a value of 150,000 counts (equivalent to 4% of all pixels) at zero but this is due to internal contrast and brightness settings within the SEM device. To ensure the thresholds were not skewed by this artifact, the black pixels were not included in the thresholding algorithm since they are known to represent void. Using the four techniques (highlighted in grey in Figure 4-5), the mean porosity of Indiana Limestone was determined to be (23±4) %.

The porosity determined using single Otsu and Ji et al.'s [20] dual Otsu thresholding method were similar, while the porosity measured using SEM was significantly higher. A potential reason for the variance between the three porosities could be due to the spatial resolution of the microCT, which was lower than the SEM spatial resolution. A lower spatial resolution implies a larger volume is averaged per voxel. Hence, a higher spatial resolution more closely approaches a linear correlation between the grayscale value and the microporosity of the imaged region.

4.4.2   Pink Dolomite

The Pink Dolomite microCT samples were assessed using the two thresholding techniques (single Otsu threshold, and Ji et al.'s [20] dual Otsu threshold; Figure 4-1b). The single Otsu threshold resulted in a porosity of (30±2) %. Using the Ji et al.'s [20] dual Otsu threshold technique, the porosity was determined to be (27±2) %.

The microCT histogram for Pink Dolomite is a gradual transition of greyscale values (Figure 4-1b). Compared to the microCT histogram of Indiana Limestone (Figure 4-1a) the Pink Dolomite microCT histogram has a smaller relative peak than Indiana Limestone, and only has a shoulder in the histogram at a lower grayscale value whereas the Indiana Limestone microCT data has two distinct peaks. The pore structure of Pink Dolomite is distinct from Indiana Limestone since there are more small pores, compared

to a broad range of pore volumes. The different grayscale histograms could indicate the microporosity of the Pink Dolomite is too far below the spatial resolution of the microCT. The Ji et al.'s [20] dual Otsu threshold technique evaluated the total porosity of Pink Dolomite as (27±2) %, shown in Figure 4-1b for a representative sample. The local microporosity in the region between Ji_1 and Ji_2 (shown in Figure 4-2), demonstrates a similar range in fraction of the total volume for the microporous region between Indiana Limestone (0.5-1.0) % and Pink Dolomite (0.7-1.2) %. However, the range in local microporosity is higher for the Pink Dolomite sample at (25-45) % than the Indiana Limestone sample at (17-35) %. This indicated that the microporosity was a larger fraction of the void space for Pink Dolomite compared to Indiana Limestone. A summary of the evaluated porosities using the three techniques is provided in Table 4-1.

To binarize the Pink Dolomite SEM, only two thresholding techniques available in Fiji image processing software [118] are applicable, due to the bimodal nature of the histogram. These two techniques were: Intermodes [138] and Minimum [138] (shown in grey in Figure 4-7). The mean porosity of these two values was (34±3) %. This demonstrates that for Pink Dolomite, single Otsu's method provided a similar measure of the total porosity when compared to the total porosity measured using SEM. Ji et al.'s [20] dual Otsu thresholding technique was lower than that measured using SEM. This indicates that even between carbonates the most appropriate thresholding technique varies between Indiana Limestone and Pink Dolomite.

The porosity measured from high resolution SEM images can be affected by the following four sources of error. First, in regions of high topographical changes, for example, at the edge of a deep pore, the scattering of the electrons can lead to regions which appear white (solid), causing the histogram to skew. Second, sample preparation artifacts, such as grinding scratches, can lead to an over estimation of the porosity. Third, contaminants to the surface can obscure the image of the material. Hence, maintaining a clean sample, free of fibers or dust is required. Fourth, mineral heterogeneity (which was not the case for Indiana Limestone and Pink Dolomite) could lead to challenges in the segmentation of the greyscale, as each mineral would have a unique greyscale profile. In this study, these sources of error were minimized or eliminated by careful sample preparation and by investigating rocks which were mono-mineral.

Converting the microCT data to binary images is a necessary and crucial step to extract the pore space from microCT grayscale image stacks. The assessment performed in this study shows that before applying a thresholding technique the spatial resolution, material, and imaging technique used must be first considered.

4.5   Conclusion

The comparison of the thresholding techniques shows the sensitivity of determined thresholds to the imaging technique, spatial resolution, and rock type investigated. For Indiana Limestone, the single Otsu threshold and Ji et al.'s [20] dual Otsu threshold methods evaluated the porosity as (13±1) % and (14±5) %, respectively. This is significantly lower than the porosity determined from a high resolution SEM image, which measured the porosity to be (23±4) %. Similarly, for Pink Dolomite, the single Otsu threshold and Ji et al.'s [20] dual Otsu threshold methods evaluated the porosity as (30±2) % and (27±2) %, respectively. Compared to the porosity determined from a high resolution SEM image, evaluated as (34±3) %, the porosity measurement was higher than both the single Otsu and Ji et al.'s [20] dual Otsu threshold methods.

Although this study was preliminary in nature, it shows that a systematic thresholding methodology for both SEM and microCT data is required. To produce a more robust thresholding methodology, it is proposed that standards be developed to calibrate grayscale histograms of SEM and microCT data. These standards should be validated for a broad range of resolutions, rock types and pore structure morphologies.

4.6   Tables

Table 4-1: Comparison of the assessed segmentation techniques for microCT data. A summary of the total porosity determined by the segmentation techniques for the Indiana Limestone and Pink Dolomite samples is shown.

Segmentation Technique	Indiana Limestone Porosity (%)	Pink Dolomite Porosity (%)
Single Otsu	(13±1)	(30±2)
Ji et al.'s [20] Dual Otsu	(14±5)	(27±2)
SEM	(23±4)	(34±3)

4.7   Figures
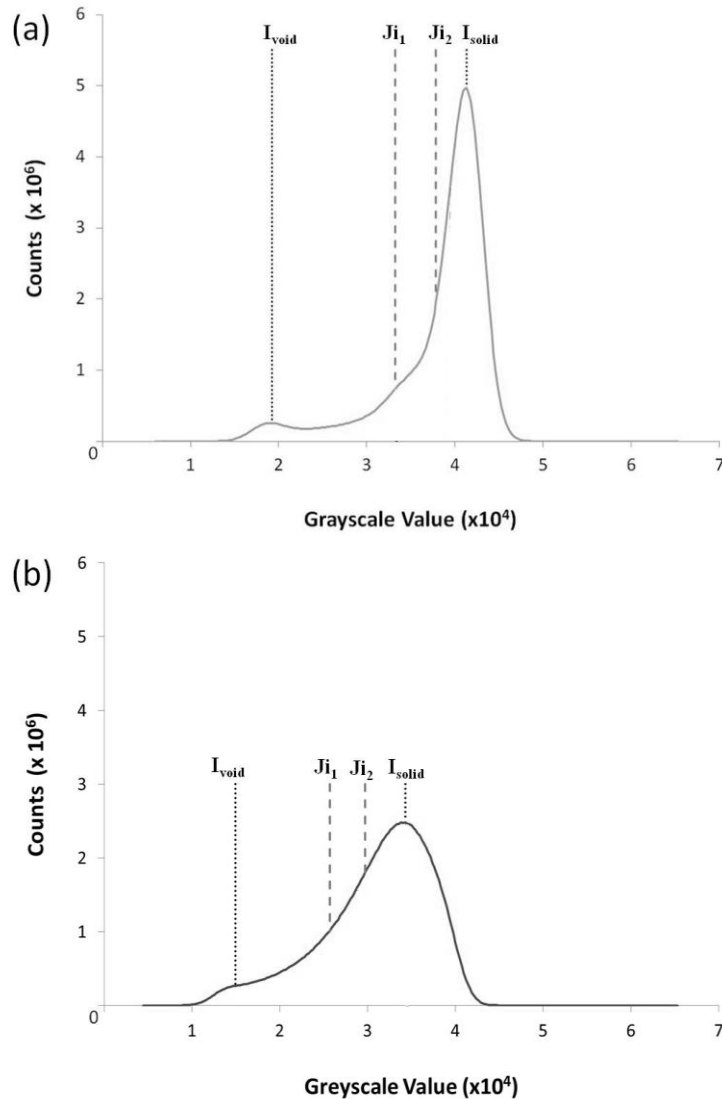
Figure 4-1: Greyscale histogram of the microCT data for Indiana Limestone a) and Pink Dolomite b). The lines 'I_{void}' and 'I_{solid}' delineate the peak of the void region and solid region, respectively. The lines Ji_1 and Ji_2 are the boundaries of the microporous region as determined using Ji et al.'s [20] dual Otsu thresholding technique.
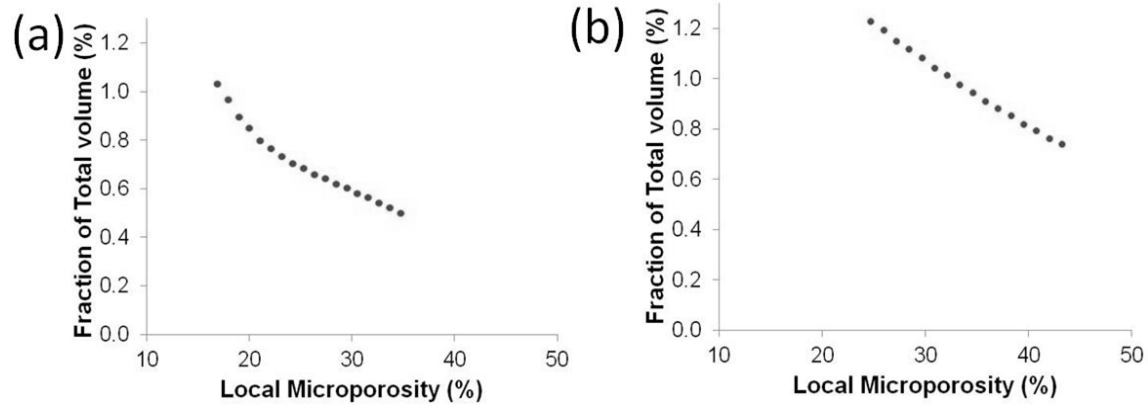
Figure 4-2: The local microporosity of the microCT data for the (a) Indiana Limestone and (b) Pink Dolomite samples in the microporous region calculated using Ji et al.'s [20] dual Otsu thresholding technique. The fraction of the total volume at a given microporosity has a similar range (0.5-1.0) % in the Indiana Limestone sample and (0.7-1.2) % in the Pink Dolomite sample.
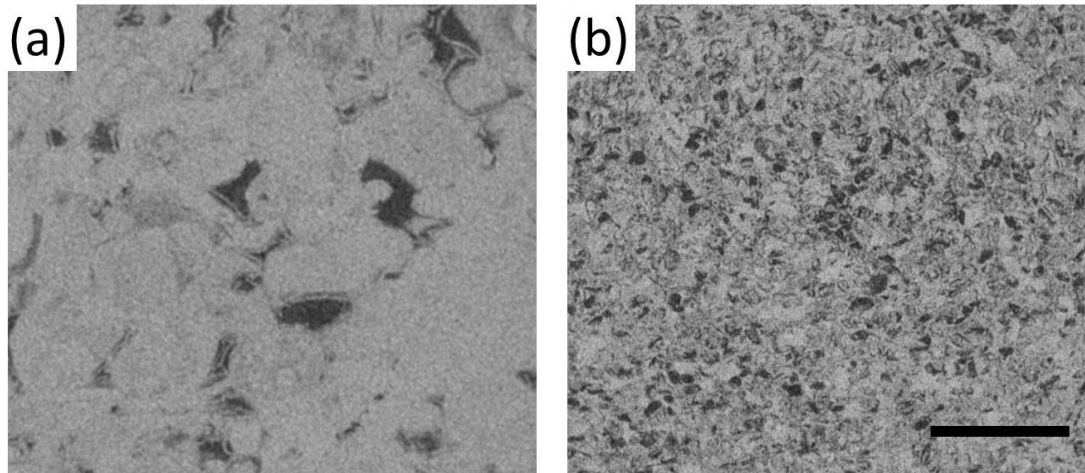
Figure 4-3: Greyscale image of (a) Indiana Limestone and (b) Pink Dolomite microCT
samples. The length bar is applicable to (a) and (b) and represents 1 mm.
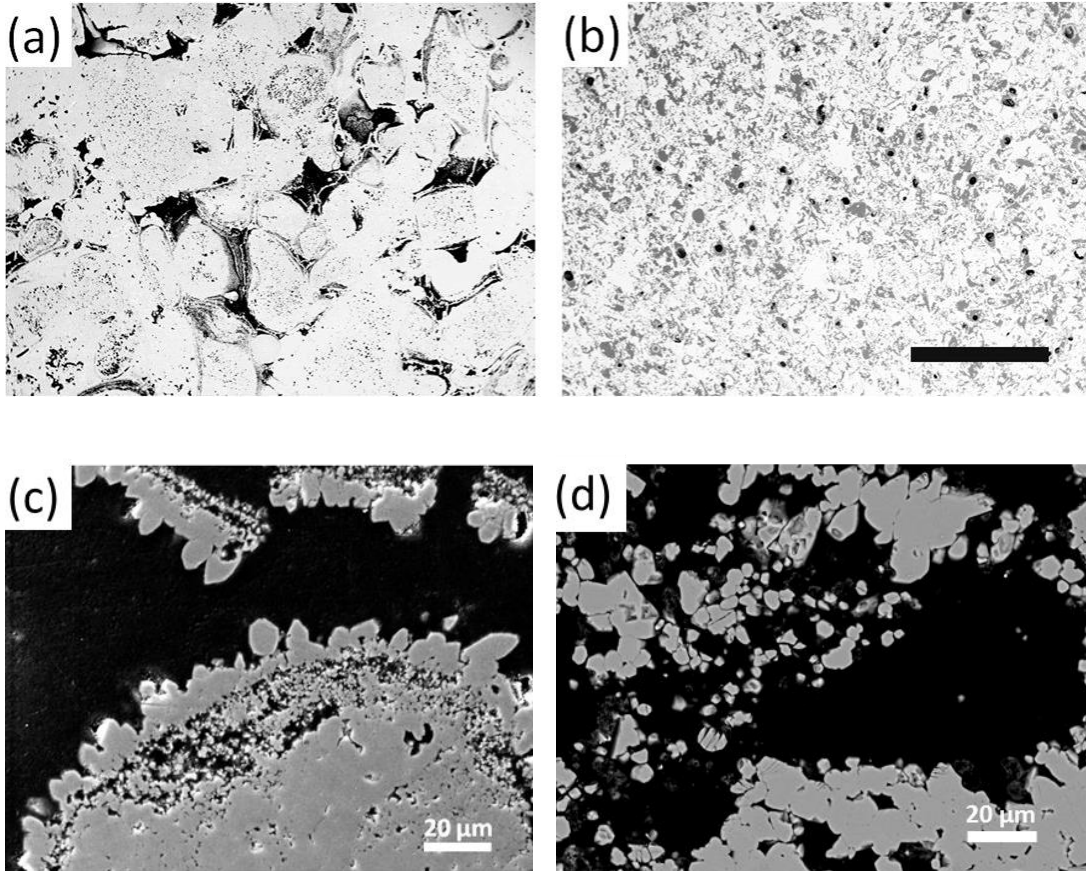
Figure 4-4: Greyscale backscattered scanning electron microscopy images of (a) Indiana Limestone and (b) Pink Dolomite. The length bar is applicable to (a) and (b) and represents 1 mm. High resolution scanning electron microscopy images of microporous regions of (c) Indiana Limestone and (d) Pink Dolomite. The length bar in (c) and (d) represents 20 μm.
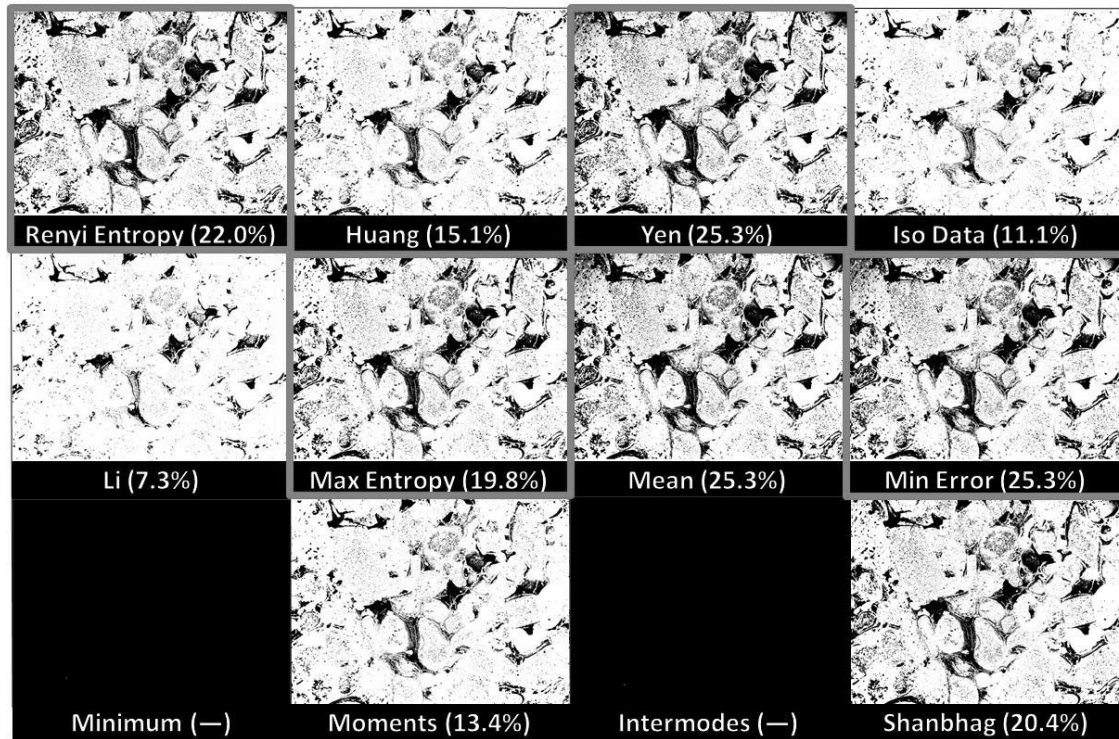
Figure 4-5: The greyscale Indiana Limestone backscattered electron scanning electron microscopy (SEM) image was converted to a binary image using the thresholding technique named below each image. The porosity of the binary image is in brackets. The four thresholding techniques, Renyi Entropy, Yen, Maximum Entropy and Minimum Error, highlighted with a grey box were selected for determining the mean porosity of the Indiana Limestone sample. Minimum and Intermodes have no recorded porosity because the thresholding techniques are for strictly bimodal histograms and the algorithm could not converge for the single peak histogram of the Indiana Limestone SEM.
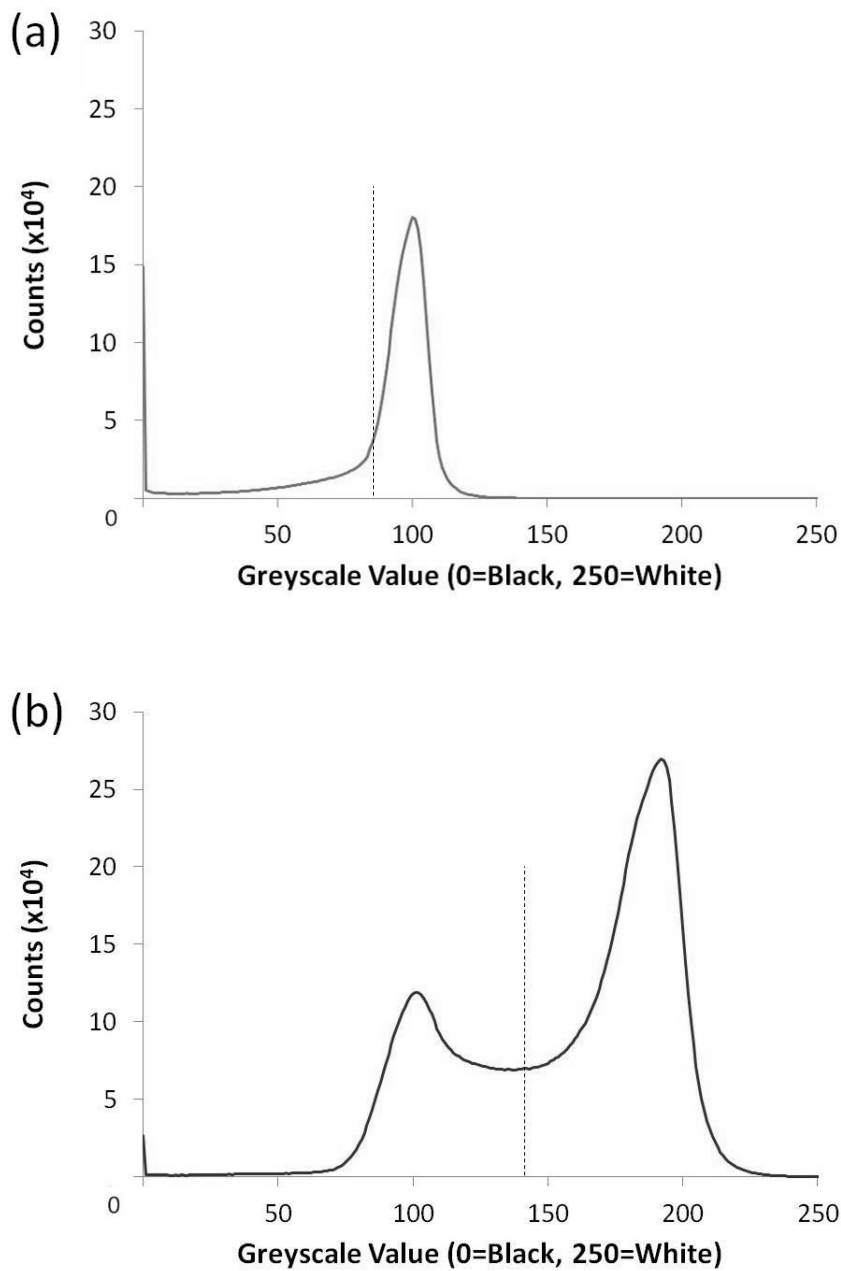
Figure 4-6: Greyscale histograms of (a) Indiana Limestone and (b) Pink Dolomite back-scattered SEM images. The dotted line in both (a) and (b) represents the threshold used to binarize the grayscale images.
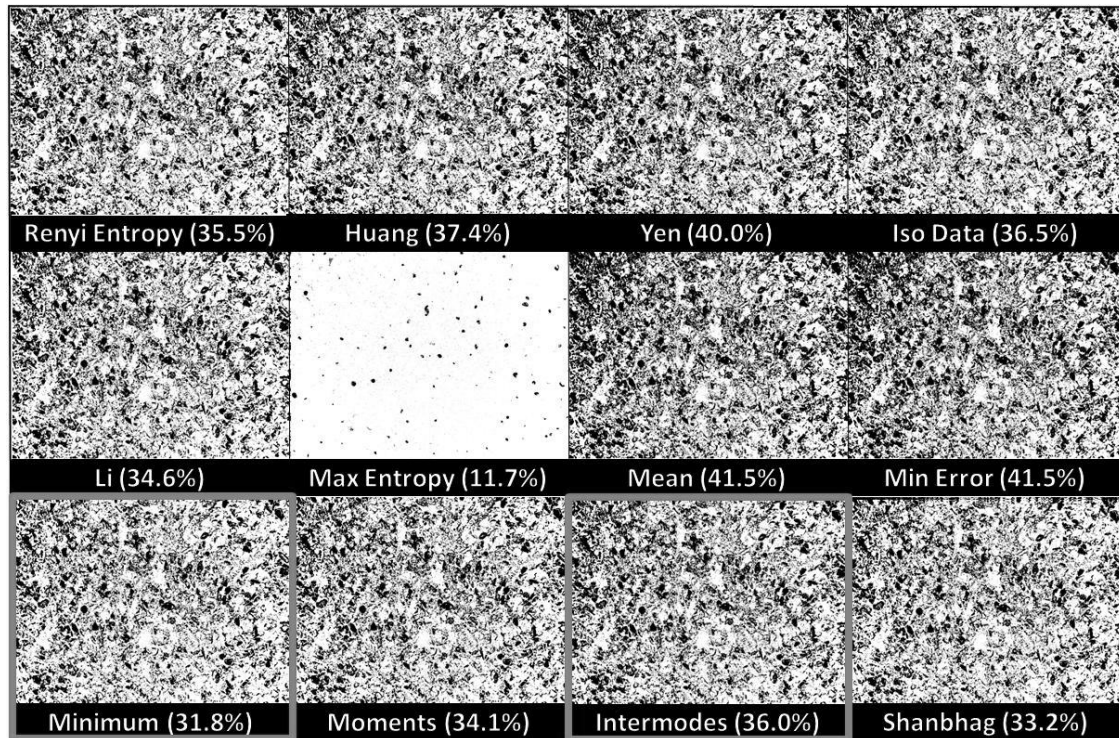
Figure 4-7: The greyscale Pink Dolomite backscattered electron scanning electron microscopy image was converted to a binary image using the thresholding technique named below each image. The porosity of the binary image is in brackets. The two thresholding techniques, Minimum and Intermodes, highlighted with a grey box were selected for determining the mean porosity of the Pink Dolomite sample.

Chapter 5
Conclusions & Future Work

5.1   Conclusions

In this thesis, Indiana Limestone and Pink Dolomite were investigated as model carbonates for their suitability as formations for carbon dioxide storage. A literature review on carbon dioxide storage technology, and the role microscale processes play in governing the transport of the injected carbon dioxide plume within the geologic formation was presented. The pore structures of the samples were analyzed using pore network models extracted from X-ray micro computed tomography (microCT) data. The dual porosity of the carbonates was also investigated to determine the sensitivity of the thresholding methods to the imaging technique, spatial resolution, and rock type of the samples.

5.1.1   Pore Structure Characterization

Statistical distributions of pore scale parameters describing the internal pore geometry were determined for two model carbonates, Indiana Limestone and Pink Dolomite, which are representative of suitable carbon dioxide storage formations. These statistical distributions are necessary as structural input parameters for pore scale and reservoir scale simulations of carbon dioxide injection into brine-filled porous rock structures to determine the carbon dioxide storage capacities of these formations. The key characteristics of the pore space that were determined include: mean pore volume, mean pore radius, mean throat radius, mean coordination number, and mean pore-to-pore distance. These characteristics can be incorporated into large-scale reservoir simulations using upscaling techniques, such as local, or global upscaling and including the porosity, and the permeability into descriptions of the flow using Darcy's law.

The lognormal distributions were found using a pore network extraction algorithm based on the Watershed algorithm. Although Pink Dolomite has not been analyzed using pore network modeling in the literature, Indiana Limestone was assessed by Gharbi et al. The results here matched well with as small as a 9% difference between Gharbi et al.'s

computed statistical characteristics and those computed for the Indiana Limestone samples.

From pore space extractions based on microCT imaging and a novel Watershed algorithm, Pink Dolomite and Indiana Limestone were characterized. The final saturations of both samples were similar, Indiana Limestone reached up to 54 % saturation and Pink Dolomite reached 56 % saturation. The preferred rock type for injection could not be determined directly from the analyses conducted as the overall permeability, heterogeneity of a reservoir and geochemical aspects would also need to be considered.

5.1.2   Mineral Characterization

The bulk mineral composition of Indiana Limestone and Pink Dolomite were determined using X-ray fluorescence as 98.6% and 99.4% calcite ($CaCO_3$) by atomic weight percent, respectively.

5.1.3   Dual Porosity of Carbonates

The porosity of Indiana Limestone and Pink Dolomite was determined from scanning electron microscopy (SEM) and microCT data to provide a comparison of the various imaging methods and thresholding techniques. In the analysis conducted here, high-resolution (0.9-1.5 μm/pixel) SEM images were thresholded using global thresholding techniques. The porosity determined was compared to the porosity and microporosity determined from lower resolution three-dimensional microCT data using Otsu's method [71] and Ji et al.'s [20] dual Otsu method.

For Indiana Limestone, the Otsu [71] threshold and Ji et al.'s [20] dual Otsu threshold methods evaluated the porosity as (13±1) % and (14±5) %, respectively. This is significantly lower than the porosity determined from a high resolution SEM image, which measured the porosity to be (23±4) %. Similarly, for Pink Dolomite, the single Otsu [71] threshold and Ji et al.'s [20] dual Otsu threshold methods evaluated the porosity as (30±2) % and (27±2) %, respectively. Compared to the porosity determined from a high resolution SEM image, evaluated as (34±3) %, the porosity was higher than both the single Otsu [71] and Ji et al.'s [20] dual Otsu threshold methods.

The contributions of this work provide a starting point for future work to determine the feasibility and potential storage capacity carbonate formations for carbon capture and storage technology.

5.2   Future Work

Based on the findings in this thesis, there are many areas of carbon capture and storage technology that can be further investigated. The pore network model that was used to determine the characteristics, pore size distribution, capillary pressure vs. volume saturation could be modified to determine the permeability, tortuosity, and specific surface area of the geologic material. Furthermore, it could see application to various other porous materials.

The pore network model and invasion percolation code which was used to determine the characteristics of the rock is also an area for future work. Extending the analysis to include geochemical reactions, such as dissolution and crystallization is a natural next step in an exhaustive analysis of a potential formation for injection of carbon dioxide for long term storage. Experimental work would need to be completed to validate the models of the geochemical reactions, and to accurately represent the complex processes which would occur within the formation upon injection of carbon dioxide.

In future studies, obtaining a higher spatial resolution of the rock structure through the use of synchrotron radiation computed tomography would provide a more detailed characterization of the pore space. One of the major findings of this thesis was that the characteristics of the pore structure are highly dependent on the type of rock that was investigated. Future work should include a larger number of samples of different rock types to fully characterize a given formation.

Furthermore, the samples investigated should be obtained from various depths of the formation. In this thesis, the samples were procured from a supplier of scientific samples, which quarried from surface to a maximum of 60 m deep. For samples more representative of carbon dioxide storage sites, depths should be on the order of 800 m or greater. This would allow for more representative samples. A larger sample set would also allow for consideration of the role depth within the formation plays on porosity,

permeability and tortuosity. A comparison can be made between the results presented in this thesis for near surface samples, and samples from deeper depths.

References

[1]   B. Metz, O. Davidson, H. de Coninck, M. Loos, and L. Meyer, Eds., *IPCC Special Report on Carbon Dioxide Capture and Storage*. Cambridge University Press, 2005, p. 443.

[2]   A. Bachu, C. Hawkes, M. Pooladi-Darvish, and E. Perkins, "CCS site selection and characterisation criteria," 2009.

[3]   F. Thauvin and K. Mohanty, "Network Modeling of Non-Darcy Flow Through Porous Media," *Transport in Porous Media*, vol. 31, no. 1, pp. 19–37, 1998.

[4]   L. Louis, P. Baud, and T.-F. Wong, "Characterization of pore-space heterogeneity in sandstone by X-ray computed tomography," *Geological Society, London, Special Publications*, vol. 284, no. 1, pp. 127–146, 2007.

[5]   G. Jin, C. Torres-Verdin, F. Radaelli, and E. Rossi, "Experimental Validation of Pore-Level Calculations of Static and Dynamic Petrophysical Properties of Clastic Rocks," *Proceedings of SPE Annual Technical Conference and Exhibition*, pp. 7–12, 2007.

[6]   P. Bhattad, C. Willson, and K. Thompson, "Effect of Network Structure on Characterization and Flow Modeling Using X-ray Micro-Tomography Images of Granular and Fibrous Porous Media," *Transport in Porous Media*, vol. 90, pp. 363–392, 2011.

[7]   D. Silin, L. Tomutsa, S. M. Benson, and T. W. Patzek, "Microtomography and Pore-Scale Modeling of Two-Phase Fluid Distribution," *Transport in Porous Media*, vol. 86, no. 2, pp. 495–515, 2010.

[8]   D. Lu, M. Zhou, J. H. Dunsmuir, and H. Thomann, "NMR T2 distributions and two phase flow simulations from X-ray micro-tomography images of sandstones.," *Magnetic resonance imaging*, vol. 19, no. 3–4, pp. 443–8, 2001.

[9]   S. M. Benson, B. Li, M. Krause, S. Krevor, C. Kuo, R. Pini, and L. Zuo, "Investigations in Geologic Carbon Sequestration : Multiphase Flow of CO 2 and Water in Reservoir Rocks," Stanford, 2012.

[10]   C. Eisinger and J. Jensen, "Reservoir Characterization for CO_2 Sequestration: Assessing the Potential of the Devonian Carbonate Nisku Formation of Central Alberta," *Oil & Gas Science and Technology – Revue d'IFP Energies nouvelles*, vol. 66, no. 1, pp. 47–65, 2011.

[11]   D. Kim, C. Peters, and W. B. Lindquist, "Upscaling geochemical reaction rates accompanying acidic CO_2-saturated brine flow in sandstone aquifers," *Water Resources Research*, vol. 47, p. W01505, 2011.

[12]   C. D. Tsakiroglou and A. C. Payatakes, "Characterization of the pore structure of reservoir rocks with the aid of serial sectioning analysis, mercury porosimetry and network simulation," *Advances in Water Resources*, vol. 23, no. 7, pp. 773–789, 2000.

[13]   E. Harel, J. Granwehr, J. a Seeley, and A. Pines, "Multiphase imaging of gas flow in a nanoporous material using remote-detection NMR.," *Nature materials*, vol. 5, no. 4, pp. 321–7, 2006.

[14]   C. M. Gribble, G. P. Matthews, G. M. Laudone, A. Turner, C. J. Ridgway, J. Schoelkopf, and P. A. C. Gane, "Porometry, porosimetry, image analysis and void network modelling in the study of the pore-level properties of filters," *Chemical Engineering Science*, vol. 66, no. 16, pp. 3701–3709, 2011.

[15]   Z. Jiang, K. Wu, G. Couples, M. I. J. van Dijke, K. S. Sorbie, and J. Ma, "Efficient extraction of networks from three-dimensional porous media," *Water Resources Research*, vol. 43, no. 12, pp. 1–17, 2007.

[16]   T. Roberts-Ashby and M. Stewart, "Potential for carbon dioxide sequestration in the Lower Cretaceous Sunniland Formation within the Sunniland Trend of the South Florida Basin, U.S.," *International Journal of Greenhouse Gas Control*, vol. 6, pp. 113–125, 2012.

[17]   E. Manrique, M. Gurfinkel, and V. Muci, "Enhanced Oil Recovery Field
       Experiences in Carbonate Reservoirs in the United States EOR in U.S. Carbonate
       Reservoirs," in *25th Annual Workshop & Symposium Collaborative Project on
       Enhanced Oil Recovery International Energy Agency*, 2004, pp. 1–32.

[18]   S. Bachu, "Sequestration of CO_2 in geological media in response to climate
       change: road map for site selection using the transform of the geological space into
       the CO_2 phase space," *Energy Conversion and Management*, vol. 43, no. 1, pp. 87–
       102, 2002.

[19]   P. Gouze and L. Luquot, "X-ray microtomography characterization of porosity,
       permeability and reactive surface changes during dissolution.," *Journal of
       contaminant hydrology*, vol. 120–121, pp. 45–55, 2011.

[20]   Y. Ji, P. Baud, V. Vajdova, and T. -f. Wong, "Characterization of Pore Geometry
       of Indiana Limestone in Relation to Mechanical Compaction," *Oil & Gas Science
       and Technology – Revue d'IFP Energies nouvelles*, vol. 67, no. 5, pp. 753–775,
       2012.

[21]   S. Galaup, Y. Liu, and A. Cerepi, "New integrated 2D–3D physical method to
       evaluate the porosity and microstructure of carbonate and dolomite porous
       system," *Microporous and Mesoporous Materials*, vol. 154, pp. 175–186, 2012.

[22]   D. Bauer, S. Youssef, M. Han, S. Bekri, E. Rosenberg, M. Fleury, and O. Vizika,
       "From computed microtomography images to resistivity index calculations of
       heterogeneous carbonates using a dual-porosity pore-network approach: Influence
       of percolation on the electrical transport properties," *Physical Review E*, vol. 84,
       no. 1, p. 111-133, 2011.

[23]   R. Agersborg, T. A. Johansen, and M. Jakobsen, "Velocity variations in carbonate
       rocks due to dual porosity and wave-induced fluid flow," *Geophysical Prospecting*,
       vol. 57, no. 1, pp. 81–98, 2009.

[24] O. Gharbi, B. Bijeljic, E. Boek, and M. J. Blunt, "Changes in Pore Structure and Connectivity Induced by CO_2 Injection in Carbonates: A Combined Pore-Scale Approach," *Energy Procedia*, vol. 37, no. 1, pp. 5367–5378, 2013.

[25] E. De Boever, C. Varloteaux, F. H. Nader, A. Foubert, S. Békri, S. Youssef, and E. Rosenberg, "Quantification and Prediction of the 3D Pore Network Evolution in Carbonate Reservoir Rocks," *Oil & Gas Science and Technology – Revue d'IFP Energies nouvelles*, vol. 67, no. 1, pp. 161–178, 2012.

[26] G. Baechle, A. Colpaert, G. Eberli, and R. Weger, "Effects of microporosity on sonic velocity in carbonate rocks," *The Leading Edge*, vol. 27, no. 8, pp. 1012–1018, 2008.

[27] M. T. Applied and B. Aquifer, "Multiple Technologies Applied to Characterization of the Porosity and Permeability of the Biscayne Aquifer , Florida," 2011.

[28] P. Baud, Y. Ji, V. Vajdova, and T. Wong, "Characterization of pore space geometry in limestones in relation to their compaction in reservoirs," in *Int. Conf. on Flows and Mechanics in Natural Porous Media from Pore to Field Scale*, 2011, pp. 1–3.

[29] D. Bauer, S. Youssef, M. Fleury, S. Bekri, E. Rosenberg, and O. Vizika, "Improving the Estimations of Petrophysical Transport Behavior of Carbonate Rocks Using a Dual Pore Network Approach Combined with Computed Microtomography," *Transport in Porous Media*, vol. 94, no. 2, pp. 505–524, 2012.

[30] B. Bijeljic, P. Mostaghimi, and M. J. Blunt, "Insights into non-Fickian solute transport in carbonates," *Water Resources Research*, vol. 49, no. 5, pp. 2714–2728, 2013.

[31] W. Zhu, P. Baud, and T. Wong, "Micromechanics of cataclastic pore collapse in limestone," *Journal of Geophysical Research*, vol. 115, no. B4, p. B04405, 2010.

[32] S. Latham, T. Varslot, and A. Sheppard, "Image registration: enhancing and calibrating X-ray micro-CT imaging," in *International Symposium of the Society of Core Analysts*, 2008, pp. 1–12.

[33] J.-C. Robinet, P. Sardini, D. Coelho, J.-C. Parneix, D. Prêt, S. Sammartino, E. Boller, and S. Altmann, "Effects of mineral distribution at mesoscopic scale on solute diffusion in a clay-rich rock: Example of the Callovo-Oxfordian mudstone (Bure, France)," *Water Resources Research*, vol. 48, no. 5, p. W05554, 2012.

[34] V. Alvarado and E. Manrique, "Enhanced Oil Recovery: An Update Review," *Energies*, vol. 3, no. 9, pp. 1529–1575, 2010.

[35] C. W. Macminn, M. L. Szulczewski, and R. Juanes, "CO_2 migration in saline aquifers. Part 1. Capillary trapping under slope and groundwater flow," *Journal of Fluid Mechanics*, vol. 662, pp. 329–351, 2010.

[36] G. Landrot, J. B. Ajo-Franklin, L. Yang, S. Cabrini, and C. I. Steefel, "Measurement of accessible reactive surface area in a sandstone, with application to CO_2 mineralization," *Chemical Geology*, vol. 318–319, no. 7, pp. 113–125, 2012.

[37] H. J. Herzog, "Scaling up carbon dioxide capture and storage: From megatons to gigatons," *Energy Economics*, vol. 33, no. 4, pp. 597–604, 2011.

[38] H. Koide, Y. Tazaki, Y. Noguchi, and M. Iijima, "Carbon dioxide injection into useless aquifers and recovery of natural gas dissolved in fossil water," *Energy Conversion and Management*, vol. 34, no. 9, pp. 921–924, 1993.

[39] W.-J. Plug and J. Bruining, "Capillary pressure for the sand–CO_2–water system under various pressure conditions. Application to CO2 sequestration," *Advances in Water Resources*, vol. 30, no. 11, pp. 2339–2353, 2007.

[40] L. Thorleifson, "Potential Capacity for Geologic Carbon Sequestration in the Midcontinent rift system in Minnesota," 2008.

[41] J. M. Nordbotten, M. A. Celia, and S. Bachu, "Injection and Storage of CO_2 in Deep Saline Aquifers: Analytical Solution for CO_2 Plume Evolution During Injection," *Transport in Porous Media*, vol. 58, no. 3, pp. 339–360, 2005.

[42] M. Thomas, M. Stewart, M. Trotz, and J. Cunningham, "Geochemical modeling of CO_2 sequestration in deep, saline, dolomitic-limestone aquifers: Critical evaluation of thermodynamic sub-models," *Chemical Geology*, vol. 306–307, pp. 29–39, 2012.

[43] J. M. Nordbotten, M. A. Celia, S. Bachu, and H. K. Dahle, "Semianalytical Solution for CO_2 Leakage through an Abandoned Well," *Environmental science & technology*, vol. 39, no. 2, pp. 602–11, 2005.

[44] R. Shukla, P. Ranjith, A. Haque, and X. Choi, "A review of studies on CO_2 sequestration and caprock integrity," *Fuel*, vol. 89, no. 10, pp. 2651–2664, 2010.

[45] M. Celia, J. Nordbotten, M. Dobossy, T. Elliot, and K. Bandilla, "Modeling Options to Answer Practical Questions for CO_2 Sequestration Operations," *Analysis*, pp. 1–19, 2011.

[46] S. Bachu, "Sequestration of CO_2 in geological media: criteria and approach for site selection in response to climate change," *Energy Conversion and Management*, vol. 41, no. 9, pp. 953–970, 2000.

[47] P. S. Ringrose and P. W. M. Corbett, "Controls on two-phase fluid flow in heterogeneous sandstones," *Geological Society, London, Special Publications*, vol. 78, no. 1, pp. 141–150, 1994.

[48] S. M. Benson and D. R. Cole, "CO_2 Sequestration in Deep Sedimentary Formations," *Elements*, vol. 4, no. 5, pp. 325–331, 2008.

[49] L. Louis, P. Baud, and T.-F. Wong, "Characterization of pore-space heterogeneity in sandstone by X-ray computed tomography," *Geological Society, London, Special Publications*, vol. 284, no. 1, pp. 127–146, 2007.

[50] S. C. M. Krevor, R. Pini, B. Li, and S. M. Benson, "Capillary heterogeneity trapping of CO_2 in a sandstone rock at reservoir conditions," *Geophysical Research Letters*, vol. 38, no. 15, pp. 1–5, 2011.

[51] S. Emberley, I. Hutcheon, M. Shevalier, K. Durocher, B. Mayer, W. D. Gunter, and E. H. Perkins, "Monitoring of fluid–rock interaction and CO_2 storage through produced fluid sampling at the Weyburn CO_2-injection enhanced oil recovery site, Saskatchewan, Canada," *Applied Geochemistry*, vol. 20, no. 6, pp. 1131–1157, 2005.

[52] F. Javadpour, "CO_2 Injection in Geological Formations: Determining Macroscale Coefficients from Pore Scale Processes," *Transport in Porous Media*, vol. 79, no. 1, pp. 87–105, 2008.

[53] P. A. Selvadurai and A. P. S. Selvadurai, "On the Surface Permeability of Indiana Limestone," vol. i, no. May, pp. 1–9, 2009.

[54] H. Dong, "Micro-CT Imaging and Pore Network Extraction," Imperial College London, 2007.

[55] M. Al-Awadi, W. J. Clark, W. R. Moore, M. Herron, and T. Zhang, "Dolomite: Perspectives on a Perplexing Mineral," *Oilfield Review*, vol. 21, no. 3, pp. 32–45, 2009.

[56] J. Owens, *Indiana Limestone Handbook*, 22nd ed. Indiana Limestone Institute of America, Inc., 2007, p. 154.

[57] A. Cerepi, "Geological control of electrical behaviour and prediction key of transport properties in sedimentary porous systems," *Colloids and Surfaces A: Physicochemical and Engineering Aspects*, vol. 241, no. 1–3, pp. 281–298, 2004.

[58] J. Goldstein, D. Newbury, D. Joy, C. Lyman, P. Echlin, E. Lifshin, L. Sawyer, and J. Michael, *Scanning Electron Microscopy and X-Ray Microanalysis*. Kluwer Adacemic/Plenum Pulbishers, 2003, p. 688.

[59] B. Bera, N. S. K. Gunda, S. K. Mitra, and D. Vick, "Characterization of nanometer-scale porosity in reservoir carbonate rock by focused ion beam-scanning electron microscopy.," *Microscopy and microanalysis the official journal of Microscopy Society of America Microbeam Analysis Society Microscopical Society of Canada*, vol. 18, no. 1, pp. 171–178, 2012.

[60] C. Hollis, V. Vahrenkamp, S. Tull, A. Mookerjee, C. Taberner, and Y. Huang, "Pore system characterisation in heterogeneous carbonates: An alternative approach to widely-used rock-typing methodologies," *Marine and Petroleum Geology*, vol. 27, no. 4, pp. 772–793, 2010.

[61] M. Ioannidis and I. Chatzis, "A mixed-percolation model of capillary hysteresis and entrapment in mercury porosimetry," *Journal of colloid and interface science*, vol. 161, pp. 278–291, 1993.

[62] W. Lindquist, "Quantitative analysis of three-dimensional X-ray tomographic images," in *International Symposium on Optical Science*, 2002, vol. 4503, pp. 103–115.

[63] D. Jerram and M. Higgins, "3D analysis of rock textures: Quantifying igneous microstructures," *Elements*, vol. 3, no. 4, pp. 239–246, 2007.

[64] G. S. Padhy, C. Lemaire, E. S. Amirtharaj, and M. A. Ioannidis, "Pore size distribution in multiscale porous media as revealed by DDIF–NMR, mercury porosimetry and statistical image analysis," *Colloids and Surfaces A: Physicochemical and Engineering Aspects*, vol. 300, no. 1–2, pp. 222–234, 2007.

[65] A. D. C. Machado, I. Lima, and R. T. Lopes, "Reservoir Rock Microstructure Evaluation by X-ray Microtomography," in *ICQNM 2012: The Sixth International Conference on Quantum, Nano and Micro Technologies*, 2012, no. 3, pp. 65–68.

[66] B. Bera, S. K. Mitra, and D. Vick, "Understanding the micro structure of Berea Sandstone by the simultaneous use of micro-computed tomography (micro-CT) and focused ion beam-scanning electron microscopy (FIB-SEM)," *Micron*, vol. 42, no. 5, pp. 412–418, 2011.

[67]   O. Gharbi and M. J. Blunt, "The impact of wettability and connectivity on relative permeability in carbonates: A pore network modeling analysis," *Water Resources Research*, vol. 48, no. 12, p. W12513, 2012.

[68]   C. A. Glasbey, G. W. Horgan, and J. F. Darbyshire, "Image analysis and three-dimensional modelling of pores in soil aggregates," *Journal of Soil Science*, vol. 42, no. 3, pp. 479–486, 1991.

[69]   W. M. Ahr, *Geology of Carbonate Reservoirs*, 1st ed. Hoboken, New Jersey: Wiley, 2008, p. 277.

[70]   D. B. McIntyre, E. E. Welday, and A. K. Baird, "Geologic application of the air pycnometer: a study of the precision of measurement," *Geological Society of America Bulletin*, vol. 76, no. 9, pp. 1055–1060, 1965.

[71]   N. Otsu, "A Threshold Selection Method from Gray-Level Histograms," *IEEE Transactions on System, Man, and Cybernetics*, vol. 9, no. 1, pp. 62–66, 1979.

[72]   A. Sufian and A. R. Russell, "Microstructural pore changes and energy dissipation in Gosford sandstone during pre-failure loading using X-ray CT," *International Journal of Rock Mechanics and Mining Sciences*, vol. 57, pp. 119–131, 2013.

[73]   H. Andrä, N. Combaret, J. Dvorkin, E. Glatt, J. Han, M. Kabel, Y. Keehm, F. Krzikalla, M. Lee, C. Madonna, M. Marsh, T. Mukerji, E. H. Saenger, R. Sain, N. Saxena, S. Ricker, A. Wiegmann, and X. Zhan, "Digital rock physics benchmarks—Part I: Imaging and segmentation," *Computers & Geosciences*, vol. 50, pp. 25–32, 2013.

[74]   M. J. Blunt, B. Bijeljic, H. Dong, O. Gharbi, S. Iglauer, P. Mostaghimi, A. Paluszny, and C. Pentland, "Pore-scale imaging and modelling," *Advances in Water Resources*, vol. 51, pp. 197–216, 2013.

[75]   Z. Jiang, M. I. J. Dijke, K. Wu, G. D. Couples, K. S. Sorbie, and J. Ma, "Stochastic Pore Network Generation from 3D Rock Images," *Transport in Porous Media*, vol. 94, no. 2, pp. 571–593, 2011.

[76] D. S. Qi and T. Hesketh, "An Analysis of Upscaling Techniques for Reservoir Simulation," *Petroleum Science and Technology*, vol. 23, no. 7–8, pp. 827–842, 2005.

[77] K. Wu, Z. Jiang, J. Ma, M. I. J. Van Dijke, and K. S. Sorbie, "Multiscale Pore System Reconstruction and Integration," in *International Symposium of the Society of Core Analysts*, 2011, pp. 1–12.

[78] D. Ushizima, G. Weber, and J. Ajo-Franklin, "Analysis and visualization for multiscale control of geologic CO_2," in *Journal of Physics: Conference Series*, 2011, pp. 1–7.

[79] A. Raoof and S. M. Hassanizadeh, "A new formulation for pore-network modeling of two-phase flow," *Water Resources Research*, vol. 48, no. 1, p. W01514, 2012.

[80] V. Joekar-Niasar and S. M. Hassanizadeh, "Analysis of Fundamentals of Two-Phase Flow in Porous Media Using Dynamic Pore-Network Models: A Review," *Critical Reviews in Environmental Science and Technology*, vol. 42, no. 18, pp. 1895–1976, 2012.

[81] C. Laroche and O. Vizika, "Two-Phase Flow Properties Prediction from Small-Scale Data Using Pore-Network Modeling," *Transport in Porous Media*, vol. 61, no. 1, pp. 77–91, 2005.

[82] J. Hinebaugh and A. Bazylak, "PEM Fuel Cell Gas Diffusion Layer Modelling of Pore Structure and Predicted Liquid Water Saturation," in *American Society of Mechanical Engineers (ASME), 9th International Fuel Cell Science, Engineering and Technology Conference, Washington DC*, 2011, pp. 1–8.

[83] C. Laroche, O. Vizika, and F. Kalaydjian, "Network modeling as a tool to predict three-phase gas injection in heterogeneous wettability porous media," *Journal of Petroleum Science and Engineering*, vol. 24, no. 2–4, pp. 155–168, 1999.

[84] B. Mayer, M. Shevalier, M. Nightingale, J. Kwon, and I. Hutcheon, "A 10-year record of geochemical and isotopic monitoring at the IEA Weyburn-Midale CO_2

Monitoring and Storage Project (Saskatchewan, Canada)," in *EGU General Assemby*, 2013, pp. 484–488.

[85] M. B. Dusseault, "Geomechanical challenges in petroleum reservoir exploitation," *KSCE Journal of Civil Engineering*, vol. 15, no. 4, pp. 669–678, 2011.

[86] J. S. Ellis and A. Bazylak, "Investigation of contact angle heterogeneity on CO_2 saturation in brine-filled porous media using 3D pore network models," *Energy Conversion and Management*, vol. 68, pp. 253–259, 2013.

[87] M. Piri and M. Blunt, "Three-dimensional mixed-wet random pore-scale network modeling of two- and three-phase flow in porous media. II. Results," *Physical Review E*, vol. 71, no. 2, p. 026302, 2005.

[88] A. S. Al-Kharusi and M. J. Blunt, "Network extraction from sandstone and carbonate pore space images," *Journal of Petroleum Science and Engineering*, vol. 56, no. 4, pp. 219–231, 2007.

[89] K. Sorbie, A. Ryazanov, and M. van Dijke, "The Structure of Residual Oil as a Function of Wettability Alteration using Pore-Scale Network Modelling," *SCA Paper A*, pp. 1–12, 2011.

[90] V. Joekar-Niasar and S. Majid Hassanizadeh, "Effect of fluids properties on non-equilibrium capillarity effects: Dynamic pore-network modeling," *International Journal of Multiphase Flow*, vol. 37, no. 2, pp. 198–214, 2011.

[91] P. Iassonov, T. Gebrenegus, and M. Tuller, "Segmentation of X-ray computed tomography images of porous materials: A crucial step for characterization and quantitative analysis of pore structures," *Water Resources Research*, vol. 45, no. 9, pp. 1–12, 2009.

[92] Q. Dou, Y. Sun, and C. Sullivan, "Rock-physics-based carbonate pore type characterization and reservoir permeability heterogeneity evaluation, Upper San Andres reservoir, Permian Basin, west Texas," *Journal of Applied Geophysics*, vol. 74, no. 1, pp. 8–18, 2011.

[93]   H. Dong and M. Blunt, "Pore-network extraction from micro-computerized-tomography images," *Physical Review E*, vol. 80, no. 3, pp. 1–11, 2009.

[94]   D. Silin, L. Tomutsa, S. M. Benson, and T. W. Patzek, "Microtomography and Pore-Scale Modeling of Two-Phase Fluid Distribution," *Transport in Porous Media*, vol. 86, no. 2, pp. 495–515, 2010.

[95]   M. Blunt, "Flow in porous media—pore-network models and multiphase flow," *Current opinion in colloid & interface science*, vol. 6, pp. 197–207, 2001.

[96]   S. Beucher and C. Lantuejoul, "Use of Watersheds in contour detection," in *Int. Workshop Image Process, Real-Time Edge Motion Detection/Estimation*, 1979, pp. 17–21.

[97]   J. B. T. M. Roerdink and A. Meijster, "The Watershed Transform: Definitions , Algorithms and Parallelization Strategies," *Fundamenta Informaticae*, vol. 41, pp. 187–228, 2001.

[98]   J. Hinebaugh and A. Bazylak, "Condensation in PEM Fuel Cell Gas Diffusion Layers: A Pore Network Modeling Approach," *Journal of The Electrochemical Society*, vol. 157, no. 10, pp. B1382–B1390, 2010.

[99]   E. M. Petriu, "Watershed segmentation for binary images with different distance transforms," *Proceedings. Second International Conference on Creating, Connecting and Collaborating through Computing*, pp. 111–116, 2004.

[100] S. Mkwelo, G. De Jager, and F. Nicolls, "Watershed-based segmentation of rock scenes and proximity-based classification of watershed regions under uncontrolled lighting conditions," in *Proceedings of 14th Annual Symposium of the Pattern Recognition Association of South Africa (PRASA)*, 2003, pp. 107–112.

[101] Y. Zhou and H. Ren, "Segmentation Method for Rock Particles Image Based on Improved Watershed Algorithm," *2012 International Conference on Computer Science and Service System*, pp. 347–349, 2012.

[102] A. Amankwah and C. Aldrich, "Rock image segmentation using watershed with shape markers," in *2010 IEEE 39th Applied Imagery Pattern Recognition Workshop (AIPR)*, 2010, pp. 1–7.

[103] P. H. Valvatne and M. J. Blunt, "Predictive pore-scale modeling of two-phase flow in mixed wet media," *Water Resources Research*, vol. 40, no. 7, pp. 1–21, 2004.

[104] S. P. Rigby, M. J. Watt-Smith, P. Chigada, J. a. Chudek, R. S. Fletcher, J. Wood, S. Bakalis, and T. Miri, "Studies of the entrapment of non-wetting fluid within nanoporous media using a synergistic combination of MRI and micro-computed X-ray tomography," *Chemical Engineering Science*, vol. 61, no. 23, pp. 7579–7592, 2006.

[105] B. Berkowitz, "Characterizing flow and transport in fractured geological media: A review," *Advances in Water Resources*, vol. 25, no. 8–12, pp. 861–884, 2002.

[106] D. Wilkinson and J. Willemsen, "Invasion percolation: a new form of percolation theory," *Journal of Physics A: Mathematical*, vol. 16, pp. 3365–3376, 1983.

[107] E. W. Washburn, "Note on a method of determining the distribution of pore sizes in a porous material," *Proceedings of the National Academy of Sciences*, vol. 7, pp. 115–116, 1921.

[108] C. J. Moon, M. K. G. Whateley, and A. M. Evans, *Introduction to Mineral Exploration*, Second. Oxford, UK: Blackwell Publishing Ltd, 2006, p. 499.

[109] M. Uchic, L. Holzer, and B. Inkson, "Three-dimensional microstructural characterization using focused ion beam tomography," *MRS Bulletin*, vol. 32, no. May, pp. 408–416, 2007.

[110] J. Hubbell, P. Trehan, N. Singh, B. Chand, D. Mehta, M. L. Garg, R. R. Garg, S. Singh, and S. Puri, "A Review, Bibliography, and Tabulation of K, L, and Higher Atomic Shell X-Ray Fluorescence Yields," *Journal of Physical and Chemical Reference Data*, vol. 23, no. 2, pp. 339–364, 1994.

[111] J. Goldstein, D. Newbury, D. Joy, C. Lyman, P. Echlin, E. Lifshin, L. Sawyer, and J. Michael, *Scanning Electron Microscopy and X-Ray Microanalysis*. Kluwer Adacemic/Plenum Pulbishers, 2003, p. 688.

[112] a. R. Kalukin, M. Van Geet, and R. Swennen, "Principal components analysis of multienergy X-ray computed tomography of mineral samples," *IEEE Transactions on Nuclear Science*, vol. 47, no. 5, pp. 1729–1736, 2000.

[113] M. J. Blunt, M. D. Jackson, M. Piri, and P. H. Valvatne, "Detailed physics, predictive capabilities and macroscopic consequences for pore-network models of multiphase flow," *Advances in Water Resources*, vol. 25, no. 8–12, pp. 1069–1089, 2002.

[114] A. Chadwick, R. Arts, C. Bernstone, F. May, S. Thibeau, and P. Zweigel, *Best Practice for the Storage of CO_2 in Saline Aquifers - Observations and Guidelines from the SACS and CO_2STORE Projects*. British Geological Survey, 2008, p. 267.

[115] P. Mostaghimi, M. J. Blunt, and B. Bijeljic, "Computations of Absolute Permeability on Micro-CT Images," *Mathematical Geosciences*, vol. 45, no. 1, pp. 103–125, 2012.

[116] J. C. Russ, *Computer-Assisted Microscopy: The Measurement and Analysis of Images*. New York: Plenum Press, 1990, p. 453.

[117] C. P. Mauer and V. Bindokas, "3D Hybrid Median Filter," 2004. [Online]. Available: http://rsbweb.nih.gov/ij/plugins/hybrid3dmedian.html.

[118] J. Schindelin, I. Arganda-Carreras, E. Frise, V. Kaynig, M. Longair, T. Pietzsch, S. Preibisch, C. Rueden, S. Saalfeld, B. Schmid, J.-Y. Tinevez, D. J. White, V. Hartenstein, K. Eliceiri, P. Tomancak, and A. Cardona, "Fiji: an open-source platform for biological-image analysis.," *Nature methods*, vol. 9, no. 7, pp. 676–82, 2012.

[119] F. E. Boas and D. Fleischmann, "CT artifacts: causes and reduction techniques," *Imaging in Medicine*, vol. 4, no. 2, pp. 229–240, 2012.

[120] S. Phan and M. K. Sen, "Porosity estimation from seismic data at Dickman Field, Kansas for carbon sequestration," in *2010 SEG Annual Meeting*, 2010, no. 1, pp. 2299–2303.

[121] A. Saeedi, R. Rezaee, B. Evans, and B. Clennell, "Multiphase flow behaviour during CO_2 geo-sequestration: Emphasis on the effect of cyclic CO_2–brine flooding," *Journal of Petroleum Science and Engineering*, vol. 79, no. 3–4, pp. 65–85, 2011.

[122] P. S. Ringrose and P. W. M. Corbett, "Controls on two-phase fluid flow in heterogeneous sandstones," *Geological Society, London, Special Publications*, vol. 78, no. 1, pp. 141–150, 1994.

[123] A. Rodrígueza-Rey, D. Argandoña, L. Calleja, L. M. Suarez del Rio, and C. Celorio, "Consolidants Influence on Sandstone Capillarity. X-ray CT Study," in in *Advances in X-ray Tomography for Geomaterials*, J. Desrues, G. Viggiani, and P. Bésuelle, Eds. London, UK: ISTE, 2010, pp. 381–387.

[124] Y. Chen and L. J. Durlofsky, "Adaptive Local-Global Upscaling for General Flow Scenarios in Heterogeneous Formations," pp. 1–26, 2004.

[125] A. Raoof, S. M. Hassanizadeh, and A. Leijnse, "Upscaling Transport of Adsorbing Solutes in Porous Media: Pore-Network Modeling," *Vadose Zone Journal*, vol. 9, no. 3, p. 624, 2010.

[126] D. Kim and W. B. Lindquist, "Dependence of Pore-to-Core Up-scaled Reaction Rate on Flow Rate in Porous Media," *Transport in Porous Media*, vol. 89, no. 3, pp. 459–473, 2011.

[127] X. H. Wen, L. J. Durlofsky, and M. G. Edwards, "Use of Border Regions for Improved Permeability Upscaling," *Mathematical Geology*, vol. 35, no. 5, pp. 521–547, 2003.

[128] Y. Chen, L. J. Durlofsky, M. Gerritsen, and X. H. Wen, "A Coupled Local-Global Upscaling Approach for Simulating Flow in Highly Heterogeneous Formations," *Advances in Water Resources*, vol. 26, no. 10, pp. 1041–1060, 2003.

[129] P.-Y. Yin, Ed., *Pattern Recognition Techniques, Technology and Applications*, no. November. Vienna, Austria: Intech, 2008, p. 626.

[130] P. Stathis, E. Kavallieratou, and N. Papamarkos, "An Evaluation Technique for Binarization Algorithms.," *Journal of Universal Computer Science*, vol. 14, no. 18, pp. 3011–3030, 2008.

[131] M. Sezgin and B. Sankur, "Survey over image thresholding techniques and quantitative performance evaluation," *Journal of Electronic Imaging*, vol. 13, no. 1, pp. 146–165, 2004.

[132] M. Dunlap and J. E. Adaskaveg, "Introduction to the Scanning Electron Microscope," 1997.

[133] N. Pal and S. Pal, "A review on image segmentation techniques," *Pattern recognition*, vol. 26, no. 9, 1993.

[134] J. Kittler and J. Illingworth, "Minimum error thresholding," *Pattern recognition*, vol. 19, no. 1, pp. 41–47, 1986.

[135] J. Kapur, P. Sahoo, and A. Wong, "A new method for gray-level picture thresholding using the entropy of the histogram," *Computer vision, graphics, and image processing*, vol. 29, pp. 273–285, 1985.

[136] P. Sahoo, C. Wilkins, and J. Yeager, "Threshold selection using Renyi's entropy," *Pattern Recognition*, vol. 30, no. 1, pp. 71–84, Jan. 1997.

[137] J. Yen, F. Chang, and S. Chang, "A new criterion for automatic multilevel thresholding," *IEEE Transactions on Image Processing*, vol. 4, no. 3, pp. 370–378, 1995.

[138] J. M. Prewitt and M. L. Mendelsohn, "The analysis of cell images.," *Annals of the New York Academy of Sciences*, vol. 128, no. 3, pp. 1035–53, 1966.